This is a preprint of a manuscript accepted in the Journal of Organic Geochemistry. Subsequent versions of this manuscript may have slightly different content.

Temperature and water depth effects on brGDGT distributions in sub-alpine lakes of mid-latitude North America

Ioana C. Stefanescu[a,*], Bryan N. Shuman[a], Jessica E. Tierney[b]

a Department of Geology and Geophysics, University of Wyoming, Laramie, WY, USA

b Department of Geosciences, University of Arizona, Tucson, AZ, USA

*Corresponding author at: Department of Geology and Geophysics, University of Wyoming, Laramie, WY 82071, USA

E-mail address: istefane@uwyo.edu (I.C. Stefanescu)

Keywords: lake sediments, 5- and 6-methyl brGDGTs, temperature calibration, mid-latitude

Abstract

Branched glycerol dialkyl glycerol tetraethers (brGDGTs) in lake sediments are increasingly being used to reconstruct past temperatures. However, recent studies suggest that brGDGT distributions and concentrations vary with lake size and environmental conditions such as seasonality and its effects on water column temperature and chemistry. To test their use as a paleothermometer in high-altitude environments of mid-latitude North America, we analyzed brGDGT distributions in lake surface sediments across a range of lake depths and elevations in the Rocky Mountains of Wyoming and Colorado. Our results suggest that brGDGT distributions and the MBT'5Me index correlate with water column temperatures, which are sensitive to both lake water depth and air temperatures. Based on these relationships, we developed a calibration to mean summer air temperatures using a Bayesian regression model that incorporates the MBT'_{5Me} index and lake water depth. We applied our calibration to lake sediments from Lower Paintrock Lake in northern Wyoming to test its use as a paleothermometer. Reconstructed temperature trends are consistent with pollen-inferred temperatures at the same site and with known regional climate history, demonstrating that our calibration can be successfully applied to infer temperatures in high-altitude environments of mid-latitude North America.

1. Introduction

Lacustrine branched glycerol dialkyl glycerol tetraethers (brGDGTs) are increasingly being used to reconstruct past mean annual air temperatures (MAAT) based on their abundances in sediment sequences [Loomis et al., 2012, Loomis et at., 2015, Miller et al., 2018, Ning et al., 2019, Feng et al., 2019]. Branched GDGTs are membrane-spanning lipids thought to be produced by bacteria living in soils, peats, freshwater and marine environments across the globe [Schouten et al., 2000, Sinninghe Damsté et al., 2000, Peterse et al., 2009, Peterse et al., 2012, De Jonge et al., 2014a, Sinninghe Damsté 2016]. The compounds were initially presumed to be synthesized by bacteria living in soils and transported to lakes and rivers via erosion [Hopmans et al., 2004], but subsequent studies found evidence that brGDGTs are being produced in the water column or in aquatic sediments [Tierney and Russell, 2009, 2010; Bechtel et al., 2010; Zhu et al., 2011; Loomis et al., 2012; Schoon et al., 2013; Zell et al., 2013, Miller et al., 2018, Martínez-Sosa and Tierney 2019]. However, the exact species of bacteria producing these compounds is still unknown [Weijers et al., 2009; Sinninghe Damsté, 2018].

The brGDGTs compounds have a core structure comprised of two ether-linked dialkyl chains [Weijers et al., 2006], with a differing number of methyl groups (4, 5, or 6) and cyclopentane rings (0, 1, or 2) [Weijers et al., 2007; De Jonge et al., 2013, 2014a]. Weijers et al., (2007) showed that the degree of methylation (the number of tetra-, penta-, or hexa-methylated brGDGTs with 4, 5, or 6 methyl groups, respectively) is related to mean annual temperatures while the degree of cyclization (the number of cyclopentane rings) is related to pH; they then defined a temperature-sensitive index of the methylation of branched tetraethers (MBT) as the ratio of the summed abundance of tetra-methylated compounds to the summed abundance of all brGDGTs and a pH-sensitive index of the cyclization of branched tetraethers (CBT) as the ratio between the sum of the most abundant cyclic compounds to the sum of the non-cyclic compounds.

Recent improvements in chromatographic separation led to the identification of isomers with methyl group positions at position $\omega/\alpha5$ or at position $\omega/\alpha6$, also referred to as 5-methyl and 6-methyl isomers [De Jonge et al., 2013, 2014a; Hopmans et al., 2016]. De Jonge et al., [2013, 2014a, 2014b] showed that the removal of 6-methyl isomers from the methylation index improves temperature calibrations. The new methylation index, MBT'_{5Me}, excludes the 6-methyl isomers [De Jonge et al., 2013] and has been calibrated to MAAT using global soil datasets [De Jonge et al., 2014b, Naafs et al., 2017b, Crampton-Flood et al., 2020], a lacustrine dataset from East Africa [Russell et al., 2018] and a global peat dataset [Naafs et al., 2017a.] However, brGDGT distributions in sediments of small, snow-fed lakes of cold mid-latitude, high-elevation settings analogous to the high latitudes have not been extensively examined.

Temperature reconstructions in cold, high-altitude environments such as the Rocky Mountain region of mid-latitude North America have been challenging to produce. Commonly used paleothermometers, such as $\delta^{18}O$ of lake carbonates, can be hard to interpret because multiple environmental factors such as the seasonality of precipitation and evapotranspiration influence the results [Leng and Marshall, 2004]. Fossil pollen has been widely used for paleothermometry in mid- to high-latitude regions [Marsicek et al., 2018], but testing ecological hypotheses related to climate change requires independent lines of evidence and some key species in the

Rocky Mountain region, in particular, have broad temperature tolerances that limit their utility [Minckley et al., 2012]. Therefore, an independent temperature proxy such as brGDGTs is needed to evaluate the temperature history of this region.

Previous studies suggest that brGDGT distributions may be seasonally biased towards late summer or fall in temperate regions [Buckles et al., 2014a, Loomis et al., 2014a, Miller et al., 2018, Dang et al., 2018] and that their concentration increases with increasing water depth [Sinninghe Damsté et al., 2009, Buckles et al., 2014a, Miller et al., 2018]. However, the relatively short summer season in high-elevation, cold environments of mid-latitude North America where snow and ice cover persist from early November to late June [Musselman, 1994, Liefert et al., 2018] can potentially influence the seasonality of lacustrine production of brGDGTs [Cao et al., 2020]. Given these considerations, the existing MBT'_{5Me} calibration for lakes in East Africa may not be universally applicable [Russell et al., 2018].

Here we present 5- and 6-methyl brGDGT distributions in modern sediments from 34 small sub-alpine lakes in the Rocky Mountains of Wyoming and Colorado. The lakes vary in elevation, mean annual air temperature, mean summer air temperature, summer water temperature, degree of stratification (i.e., surface versus bottom temperature differences), and water depth (Table 1). Our results indicate that the bacteria synthesizing these compounds are sensitive to summer lake water column temperatures, which depend upon interactions of air temperature and lake depth. Based on these results, we develop a regional calibration to summer air temperatures using a Bayesian regression model that incorporates both mean summer air temperature and water depth as predictors for the methylation index

(MBT'_{5Me}). We then apply the calibration to lake sediments spanning the last 14 kyr from Lower Paintrock Lake in northern Wyoming to test its use as a paleothermometer.

2. Methods

2.1 Study sites

We collected modern surface sediments from 34 lakes located in northern Colorado and Wyoming (Fig. 1). Of these, 21 lakes were sampled in the Medicine Bow Mountains, southern Wyoming, during July-September 2017 when these lakes experience maximum water temperatures [Musselman 1994, Liefert et al., 2018]. We also incorporated samples previously collected from three lakes in the Bighorn and Beartooth Mountains in northern Wyoming [Shuman and Serravezza, 2017] and ten additional samples from lakes in the nearby Park Range, Colorado, collected during the summers between 2010 and 2016 [Calder et al., 2015]. They expand our dataset, but do not have accompanying water temperature data. Two of the northern lakes (Duncan and Rainbow Lakes) were sampled at different water depths [Shuman and Serravezza, 2017] and Round Lake (southern WY) was sampled twice in 2017 at similar water depths, which enabled intra-lake comparisons of brGDGTs. Duncan Lake was sampled at depths of 0.95, 1.16 and 1.78 m, Rainbow Lake was sampled at depths of 1, 1.4, and 2.5 m, and Round Lake was sampled twice at a constant depth of 1.2m. Altogether, we analyzed 39 surface sediment samples.

All samples were collected in polycarbonate core tubes lowered by hand either using coring rods or rope, and the upper 1 cm of sediment was preserved for analysis. Summer water column temperatures were measured at 17 lakes in the

Medicine Bow Mountains (Table 1) while dissolved oxygen concentrations and pH were measured at 16 of these lakes (Supplementary Table 1). Mean annual air and mean summer air temperature data for each lake was obtained using the Parameter-Elevation Regressions on Independent Slopes Model (PRISM) with a resolution of 800 meters from the Climate Group at Oregon State University [Prism Climate Group, 2018]. Mean annual air temperature (MAAT) was calculated using 30-year averages (1981-2010) and mean summer air temperature (JJAS) was calculated by averaging the 30-year monthly averages of June, July, August and September.

We use JJAS as a representative air temperature in the statistical comparisons because our lake water temperature measurements also represent summer conditions. Our results are interchangeable whether we use MAAT or JJAS because both correlate with elevation in our calibration dataset (Table 2) and we do not have statistical power to separate one from the other. Our use of JJAS is consistent, however, with previous work. Lacustrine and soil brGDGT distributions in mid-latitude, temperate regions are seasonally biased towards late summer or fall [Buckles et al., 2014a, Loomis et al., 2014a, Miller et al., 2018, Dang et al., 2018; Crampton-Flood et al. 2020]. Our lakes also remain frozen for most of the year (October to early June) and, during the ice-cover season, lake water temperatures remain near 4 °C while air temperatures can drop well below 4 °C [Musselman 1994; Liefert et al., 2018; see also Cao et al., 2020].

A sediment core from Lower Paintrock Lake, Wyoming (44.390 N, 107.380° W, 2808 m elevation), collected using a hand-driven piston corer with 70 mm polycarbonate tubes, was used to test the application of the brGDGT analyses (Fig. 1, diamond). Lower Paintrock Lake (LPR) is a small moraine-dammed lake surrounded by dense lodgepole pine (*Pinus contorta*) forest, dry sagebrush (*Artemisia* spp.) meadows, and riparian areas dominated by willow (*Salix* spp.). Lily pads (*Nuphar polysepala*) grow in shallow areas of the lake, which formed in an area of Archean gneiss, quartz diorite, and quartz monzonite behind the Pinedale-age (Last Glacial Maximum) terminal moraines at the head of Paintrock Creek [Green and Drouillard, 1994]. Fossil pollen provide a record of vegetation changes at the site, which include modest shifts in the relative abundances of the conifer tree taxa during the Holocene (Rust and Minckley, 2020). Streams flow into and out of the lake, which has an area of 9.38 ha and a maximum depth of 5.8 meters. MAAT and JJAS at LPR equal 0.6 and 10°C respectively (Table 1).

The 4.63 m core from LPR was obtained at a water depth of 5.7 m near the center of the lake and was subsampled at 1 cm increments. Sub-samples were sealed in sterile whirl-pak bags and stored at 4 °C. We analyzed 36 samples for brGDGT distributions at intervals of ~11.5cm (sampling interval mean: 11.5 cm, std: 5.4 cm). The age model was derived from 12 radiocarbon dates (Supplementary Table 2) calibrated to calendar years using the *bchron* package in R (Supplementary Fig. 1), which models sediment accumulation based on a Bayesian model accounting of the radiocarbon ages using the INTCAL 13 calibration curve [Parnell et al., 2008]. For this study, we accounted for the rate of sediment deposition to infer the Holocene change in water depth at LPR (Fig. 9).

2.2 BrGDGT analysis

Lipids were extracted from 2-8 g of freeze-dried sediment using an Accelerated Solvent Extractor (ASE Dionex 350) at the University of Wyoming with dichloromethane: methanol (9:1, volume:volume, hereafter v:v). The total lipid extract was separated over an aminopropyl (LC-NH2) solid phase column using DCM: Isopropanol (2:1, v:v) then re-dissolved in Hexane and separated over silica gel columns using Hexane, DCM and MeOH to isolate the aliphatic hydrocarbon, ketone, and polar fractions respectively. The polar fraction, containing the GDGTs, was re-dissolved in Hexane:Isopropanol (99:1, v:v) and filtered through 0.45 μm polytetrafluoroethylene filters prior to analysis. BrGDGT analyses were performed using the methodology of Hopmans et al., [2016] on an Agilent 6210 single quadrupole mass spectrometer coupled to a 1260/1290 Infinity high-performance liquid chromatograph and fitted with two BEH HILIC silica columns (2.1 x 150 mm, 1.7 μm, Waters) at the University of Arizona. To assess instrumental precision, 37% of the samples were analyzed in duplicate. Average duplicate standard deviation was 0.001 for the MBT'$_{5Me}$ index. Peaks were identified manually based on comparison with the C46 internal standard (Huguet et al., 2006) and integrated automatically using the ORganIc Geochemistry peAk Integration package [Fleming and Tierney, 2016].

2.3 Mathematical analysis and notations

The individual brGDGT compounds are symbolized with the prefixes I, II and III representing compounds with 4, 5 or 6 methyl groups, respectively (also referred to as tetra-, penta- and hexa-methylated compounds) and are followed by the suffixes a, b, or c representing 0, 1 and 2 cyclopentane rings, respectively. Isomers are represented using the same nomenclature, but with a prime variant to designate the 6-methyl isomers (').

Fractional abundance f(i) of each brGDGT compound (i) is defined as follows and includes both 5- and 6-methyl isomers:

$f(i) = i / (Ia+Ib+Ic+IIa+IIa'+IIb+IIb'+IIc+IIc'+IIIa+IIIa'+IIIb+IIIb'+IIIc+IIIc')$

where i varies from Ia, Ib, etc, as mentioned above. Accordingly, the fractional abundances of tetra-, penta- and hexa-methylated compounds are defined as the ratio of the summed individual abundances of a-c compounds (including isomers for each group of compounds: I, II and III) to the summed abundances of all compounds.

The MBT'$_{5Me}$ and CBT' indices were calculated as in De Jonge et al. [2014a]:

$MBT'_{5Me} = (Ia + Ib + Ic) / (Ia + Ib + Ic + IIa + IIb + IIc + IIIa)$

$CBT' = \log_{10}[(Ic + IIa' + IIb' + IIc' + IIIa' + IIIb' + IIIc') / (Ia + IIa + IIIa)]$

All of our statistical treatments of the data were completed using base functions in R and MATLAB [R Core Team, 2018, The MathWorks, Inc.]. To account for uncertainties in each of our calibration model parameters (air temperature, water depth and MBT'$_{5Me}$), we chose a Bayesian approach as in Tierney and Tingley [2014], Tierney et al. [2019] and Crampton-Flood et al. [2020]. The Bayesian regression model is fully described in Crampton-Flood et al. [2020].

To infer the regression parameters between the MBT'$_{5Me}$ index and the environmental predictor variables, we use a model of the form:

$Y = X\beta + \varepsilon$

$\varepsilon \sim N(0,\sigma^2)$

where Y is a n-length vector of MBT'_{5Me} values with n as the number of samples. X is a n x E+1 matrix containing corresponding values of E number of environmental predictor variables and a vector of ones to represent the intercept. β is a vector of E+1 length containing the regression parameters, while ε (n-length vector) is a normally distributed error term centered around zero with variance σ^2.

Pollen-inferred temperatures at Lower Paintrock Lake were reconstructed using pollen data from Rust and Minckley [2020] and the methods of Parish et al., [2020]. The cross-correlation function (CCF) between the brGDGT- and pollen-inferred JJAS reconstructions was calculated by accounting for serial autocorrelation and uneven sample spacing using the BINCOR package in R [Polanco-Martinez et al., 2019].

3. Results

3.1 Relationships among modern environmental variables

Our dataset contains lake surface sediments from 34 small alpine lakes (<20 ha) which range from 0.5 to 25 m in depth, -0.8 to 2.6 °C in mean annual air temperature (hereafter MAAT), 8.2 to 12 °C in mean summer temperature (JJAS), and from 2701 to 3350 m in elevation (Table 1). Water column temperatures were measured at 17 of these lakes across a similar range of water depth and environmental temperatures; they showed that summer lake surface temperatures (T_{SURF}) range from 12.2 to 20.6 °C and summer lake bottom temperatures (T_{BOT}) range from 4.2 to 20.1 °C. Lakes shallower than 7 meters are well mixed in late summer with an average temperature difference of 1.6 °C between surface and bottom waters while lakes deeper than 7 meters show an average temperature difference of 7.2 °C.

We analyzed correlations among environmental variables that may control the local water temperatures (Table 2). First, both MAAT and JJAS at each lake correlated with elevation. T_{SURF} also showed a similar correlation with both elevation, MAAT and JJAS. The relationships extended further to T_{BOT}, which correlate with T_{SURF}, elevation, MAAT and JJAS. However, water depth also mediates and correlates with both T_{SURF} and $T_{BOT.}$ The average water column temperatures also strongly correlate with T_{SURF}, T_{BOT}, MAAT, JJAS, water depth and elevation. No significant correlation was found between water depth and elevation, MAAT or JJAS.

We measured water column dissolved oxygen concentrations (DO) and pH at 16 of the lakes where water temperatures were also recorded (water depths range from 0.5 to 16.2 m; Supplementary Table 1). DO in surface waters (DO_{SURF}) range from 5.6 to 8.7 mg/L and from 0.01 to 12.1 mg/L in bottom waters (DO_{BOT}). Anoxic conditions (DOC< 1mg/L) were found in the bottom waters of four lakes with water depths >7m, low DO of 3.2 and 3.7 mg/L waters were found in bottom waters of two lakes (water depths of 16.2 and 9.9 m, respectively), while all other lakes had well oxygenated waters throughout the water column with a DO range of 5.2-12.1 mg/L. The pH of the surface waters (pH_{SURF}) ranges from 6.8-9.6 and from 6.0 to 9.7 in bottom waters (pH_{BOT}) suggesting that most of our lakes are alkaline.

We analyzed correlations among environmental variables that may influence DO (Table 2) and found a strong positive correlation between DO_{BOT} and T_{BOT} and a strong negative correlation between DO_{BOT} and water depth. Furthermore, DO_{BOT}

also correlates with T_{SURF} and average water temperatures. No statistically significant correlations were found between DO_{SURF} and DO_{BOT} or between DO_{SURF} and any of the environmental variables (Table 2). DO_{BOT} is also significantly correlated to $pH_{BOT,}$ which further correlates with water depth, MAAT, JJAS, average water temperature, T_{BOT} and elevation. The pH_{TOP} shows no significant correlation to any of the environmental variables (Table 2).

3.2 BrGDGT analysis of modern lake sediment

The brGDGT compounds with the highest fractional abundances in the lake surface sediment samples (Fig. 2a) are: (1) compound IIIa with a mean of 0.26 (σ = 0.09), (2) compound IIa with a mean of 0.26 (σ = 0.05) and (3) compound Ia with a mean of 0.18 (σ = 0.06). This relative abundance pattern of increasing fractional abundance with increasing methylation for the 5-methyl isomers of the non-cyclic brGDGTs (Ia<IIa<IIIa) is most evident in sediment samples collected at water depths >3m (Fig. 2b). Conversely, in sediment samples collected at water depths <3 m, compound IIIa displays a lower fractional abundance as compared to IIa and Ia (Fig. 2c). Although some samples had low concentrations of bicyclic brGDGT compounds (IIc, IIc', IIIc and IIIc'), we achieved full separation of 5- and 6-methyl brGDGTs in all lake surface sediments as well as in the down core samples from LPR. Abundances were too low for compound IIc to be reliably quantified in 5% of the samples, for compound IIc' in 25% of the samples, for compound IIIc in 57% of the samples and for compound IIIc' in 67% of the samples.

The resulting MBT'_{5Me} values range from 0.10 to 0.40 with a mean of 0.27 and σ = 0.08 across lake surface sediment samples (Fig. 3, Table 1). We found a negative relationship between water depth and the MBT'_{5Me} index (Spearman correlation =-0.83, p<0.001) where lakes sampled at water depths <3m show higher MBT'$_{5Me}$ values than lakes sampled at water depths >3m (Fig. 3, Table 3). At constant sampling depth (e.g., at a depth of 6 m in Fig. 3), the MBT'$_{5Me}$ values are a function of elevation.

We compared the grouped fractional abundances of tetra-, penta- and hexa-methylated compounds with JJAS, T_{SURF}, and T_{BOT} for 17 surface sediment samples where these variables were measured (Fig. 4). T_{BOT} best explains the variations of all three grouped fractional abundances including tetra-methylated compounds (Spearman's r=0.83; p<0.001), penta-methylated compounds (Spearman's r=0.68; p=0.003) and hexa-methylated compounds (Spearman's r=-0.79; p<0.001). JJAS and T_{SURF} show statistically significant correlations with the summed fractional abundances of tetra- and hexa-methylated compounds (Fig. 4a,b) and no statistically significant correlations with penta-methylated compounds (p-values of 0.089 and 0.128, respectively). Moreover, the fractional abundances of the grouped tetra- and penta-methylated compounds show a positive relationship to JJAS, T_{SURF}, and T_{BOT}, and a negative relationship to water depth (Fig. 4, colored palette). Conversely, the fractional abundances of the grouped hexa-methylated compounds show a negative relationship to JJAS, T_{SURF}, and T_{BOT}, and a positive relationship to water depth (Fig. 4, colored palette).

The elevation and water depth influence on the MBT'$_{5Me}$ index are also observed in sediment samples collected at different water depths within individual lakes (Fig. 5). MBT'$_{5Me}$ values are higher by an average of 0.11 in sediments collected at Duncan Lake (elev. 2800m) versus Rainbow Lake (elev. 3000m), while the MBT'$_{5Me}$ index of intra-lake sediment samples is inversely related to water depth. MBT'$_{5Me}$ values at Duncan Lake decrease by an average of 0.07 between sediments collected at 1, 1.5 and 2 m depth. In comparison, MBT'$_{5Me}$ values at Rainbow Lake decrease by an average of 0.02 between sediments collected at 1, 1.5 and 2.5 m depth. Furthermore, samples collected at the same water depth (Round Lake, depths of 1.2 m) exhibit an insignificant difference in MBT'$_{5Me}$.

We also compared the grouped fractional abundances of tetra-, penta- and hexa-methylated compounds with the DO_{BOT} for the 16 surface sediment samples where DO was measured. DO_{BOT} is positively correlated to the MBT'$_{5Me}$ index (Table 3), to the grouped tetra-methylated compounds (Spearman's r=0.59; p=0.018) and penta-methylated compounds (Spearman's r=0.65; p=0.008) and negatively correlated to the grouped hexa-methylated compounds (Spearman's r=-0.68; p=0.005). No significant correlations were found between DO_{SURF} and any of the grouped fractional abundances or the MBT'$_{5Me}$ index (Spearman's r<0.16, p>0.05). Even though DO_{BOT} correlates with the grouped fractional abundances and with the MBT'$_{5Me}$ index, a multivariate linear regression model that includes DO_{BOT} and T_{BOT} as predictors for the MBT'$_{5Me}$ index shows that DO_{BOT} is not a significant predictor for the MBT'$_{5Me}$ index (regression coefficient on DO_{BOT}=0.0006, p=0.915).

We find that surface and bottom water pH are not significantly correlated to the CBT' index (Table 3). Furthermore, except for a significant correlation between bottom water pH and the fractional abundance of compound IIIa (Spearman's r=-0.70, p=0.004), no significant correlations were found between surface or bottom water pH and the fractional abundance of any of the other individual 5- and 6-methyl compounds.

As with the individual groups of compounds (Fig. 4), we regressed the MBT'_{5Me} index against JJAS, T_{SURF}, and T_{BOT} for all lakes as well as just shallow or deep lakes (Fig. 6). Consistent with the other results, shallow lakes exhibit much higher MBT'_{5Me} values than deep lakes; significantly distinct regression lines were calculated for shallow and deep lakes (Fig. 6, dashed lines). If water depth is excluded (Fig. 6, black solid lines), the strongest relationship is found between the MBT'_{5Me} index and T_{BOT} (Fig. 6c: adjusted $r^2=0.63$, $p<0.001$, n=17; all depths). However, only weak relationships are found between the MBT'_{5Me} index and JJAS or T_{SURF} when we do not account for water depth (Fig. 6a,b black solid lines: adjusted $r^2 = 0.03$ and 0.31, respectively).

3.3 BrGDGT calibration to summer lake bottom temperatures

Summer lake bottom temperatures (T_{BOT}) integrate influences of both water depth and JJAS and show a strong relationship to the MBT'_{5Me} index at the 17 of lakes where we measured T_{BOT} (Fig. 6c). A Bayesian regression model fit to the MBT'_{5Me} data with T_{BOT} as the predictor indicates a significant relationship:

$$MBT'_{5Me} = 0.015\ (\pm 0.003) * T_{BOT}(°C) + 0.07(\pm 0.04)$$

and error $\sigma^2=0.003\ (\pm 0.001)$

where the coefficients and their uncertainties represent the mean and one standard deviation of 4500 iterations of possible slope, intercept and error values generated by the Bayesian regression model.

To predict T_{BOT} from MBT'_{5Me} values, we invert the calibrated relationship between MBT'_{5Me} and T_{BOT}. This step requires a prior mean on T_{BOT} which we set as the mean of T_{BOT} at our sites (11.5°C) and a prior standard deviation, which we set to two times the standard deviation of T_{BOT} at our sites (2σ=9.2 °C) to ensure a range of variance suitable for the expected predictions.

The observed versus predicted values of T_{BOT} plot along the 1:1 reference line (Fig. 7) with no trend in the residuals (Spearman's r=-0.24, p=0.357). The RMSE of predicted T_{BOT} is 2.8 °C. None of the points were identified as statistical outliers, but two of the samples (East Glacier and Hourglass lakes, Fig. 7) represent large departures from the mean relationship.

3.4 Calibration of brGDGTs to summer air temperatures

T_{BOT} is correlated with JJAS and water depth and multivariate linear model (T_{BOT} = JJAS + ln(water depth)) indicates a significant relationship (adjusted r^2=0.74, p<0.001). Therefore, we also developed a Bayesian model to calibrate MBT'$_{5Me}$ to JJAS by accounting for water depth. We use log-transformed water depth as a predictor variable because the relationship between water depth and the MBT'$_{5Me}$ index is nonlinear (Fig. 3).

The Bayesian calibration model for MBT'$_{5Me}$ as a function of both summer air temperature (JJAS) and ln(water depth) at mid-latitude, high-elevation North America is:

MBT'$_{5Me}$= 0.026 (± 0.007) * JJAS °C - 0.065 (± 0.007) * ln(water depth in meters) + 0.10 (± 0.07)

and error σ^2=0.002 (±0.0005)

where the coefficients and their uncertainties represent the mean and one standard deviation of 4500 iterations of possible slope, intercept and error values generated by the Bayesian regression model.

The observed versus predicted values of MBT'$_{5Me}$ plot along the 1:1 reference line (Fig. 8a). However, residuals in the relationship (Fig. 8a) retain a correlation that might suggest the importance of an additional unconstrained variable (Spearman's r=-0.41, p=0.01).

To predict JJAS from MBT'$_{5Me}$ values and ln(water depth) values, we invert the relationship between MBT'$_{5Me}$, JJAS, and ln(water depth). The prior mean and standard deviation on JJAS was set to the mean of JJAS at our sites (10 °C) with a large standard deviation (5 °C) to ensure a range of variance suitable for the expected predictions.

The observed versus predicted values of JJAS plot along the 1:1 reference line (Fig. 8b) with no trend in the residuals (Spearman's r=-0.12, p=0.459). The RMSE of predicted JJAS is 1.3 °C. We also inverted the Bayesian model to predict ln(water depth) to assess the model performance. The observed versus predicted values of ln(water depth) also plot along the 1:1 reference line (Fig. 8c) with no trend in the residuals (Spearman's r=-0.18, p=0.263). The RMSE of predicted ln(water depth) is 0.62 (or 1.9 m). LPR plots on the 1:1 lines of observed versus predicted MBT'$_{5ME}$, JJAS and ln(WD) (Figure 8, red points), which indicates the applicability of the model to downcore reconstructions from LPR.

For comparison, we also applied the previously published calibration for MAAT based on lake surface sediments from East Africa [Russell et al., 2018] to our MBT'_{5Me} results, but the inferred temperatures of 2.0 to 12.9 °C overestimate MAAT at our lakes (Table 1). Similarly, the existing calibration for mean April-October temperatures for cold regions from lakes in China [Dang et al., 2018] reconstructed temperatures with an unreasonable range of -7.3 to 13.4 °C (Table 1).

3.5 BrGDGT analysis of downcore sediment at Lower Paintrock Lake, WY

The brGDGT compounds with the highest fractional abundances in the downcore sediment samples are: (1) compound IIa with a mean of 0.25 ($\sigma = 0.05$), (2) compound IIIa with a mean of 0.22 ($\sigma = 0.05$) and (3) compound Ia with a mean of 0.22 ($\sigma = 0.05$). The MBT'_{5Me} values range from 0.21 to 0.41 (Supplementary Table 3) with a mean of 0.32 ($\sigma = 0.05$). Abundances were too low for compound IIc' to be reliably quantified in 14% of the samples and for compound IIIc' in 50% of the samples in the downcore sediment from LPR.

3.6 Application of the JJAS and T_{BOT} calibrations at Lower Paintrock Lake, WY

The Holocene trend in reconstructed summer air temperatures inferred from the brGDGTs at LPR (Fig. 9c, black line; Supplementary Table 3) is broadly consistent with that inferred from pollen at the same site (Figure 9c, orange line). However, the absolute temperatures differ. The latest Holocene brGDGT sample (i.e., core top) indicates a JJAS temperature 2.4 °C cooler than inferred from the pollen, although the modern JJAS predicted by PRISM for LPR (10 °C, Table 1) falls within the uncertainty of both reconstructions (Fig. 9c). By contrast, the mean JJAS inferred from Holocene brGDGTs samples older than 1000 B.P. equals 14 °C, which is 2.8 °C warmer than the mean JJAS inferred from the pollen for the same period (Fig. 9c). The two timeseries correlate significantly when the upper two samples have been excluded from the brGDGT reconstruction (cross correlation function, CCF; $r_{x,y}$ =0.624 at 95% C.I., lag=0), but the inclusion of the top samples reduces the correlation ($r_{x,y}$ =0.283 at 95% C.I., lag=0). No significant CCF correlations were found at other lags. Because JJAS and MAAT co-vary across Rocky Mountain calibration sample sets for both pollen and brGDGTs, an alternative model based on MAAT also yields a reconstruction consistent with the pollen data; Supplementary Fig. 2, Supplementary Table 4).

The brGDGTs reconstruct JJAS trends consistent with the pollen-inferred reconstruction and the known forcings despite the absolute temperature offset (Figure 9a,c). The record indicates warming from 14 ka to mid-Holocene (ΔT=3.9 °C; Fig. 9a) consistent with the regional climate effects of the retreat of the Laurentide Ice Sheet (LIS) [Dyke A. 2004]. A subsequent cooling trend persists until present (ΔT=4.6 °C) consistent with decreasing summer insolation anomalies in the northern hemisphere (Fig. 9a) [Berger and Loutre, 1991]. We focus on the long-term trends because of the low temporal sampling resolution and age uncertainties, but additional millennial variability is also present in the record including during the mid- and late-Holocene. Both the brGDGTs and pollen indicate Holocene temperature maxima at ca. 8 and 5.5 ka (Fig. 9c).

The difference between the brGDGT and pollen-inferred JJAS reconstructions in the youngest samples parallels another unexpected pattern in the brGDGT- derived JJAS reconstruction, which yields temperatures for the late-Pleistocene that are 3.1 °C higher than indicated by our most recent samples (Fig. 9c, black line). During the cold Younger Dryas interval (12.7-11.6 ka), reconstructed

JJAS temperatures are 1.8 °C higher than estimated from the core top samples (Fig. 9c).

If we reconstruct lake bottom temperatures instead of air temperatures for the Holocene from LPR (Fig. 9b), the reconstruction falls within the range of lake bottom temperatures observed today during the summer at our other sites (Table 1). If the data are interpreted to represent T_{BOT} instead of JJAS, then the reconstruction indicates a similar long-term pattern with a warming trend from 14 ka to mid-Holocene (ΔT=7.6 °C) followed by a subsequent cooling trend until present (ΔT=10.5 °C). As with the JJAS reconstruction, the T_{BOT} reconstruction also yields lower-than-Pleistocene temperatures for the most recent samples (Fig. 9b).

4. Discussion

4.1 Lacustrine BrGDGTs and temperatures in mid-latitude mountain ranges

Previous analyses using brGDGT distributions suggest a relationship to MAAT in regions with limited temperature seasonality or when the dataset covers a wide geographical region with a large range of MAATs [Russell et al., 2018; Dang et al., 2018]. However, our study represents a region with substantial temperature seasonality that spans a small range of MAAT (-0.9 to 2.6 °C) and JJAS (8.2 to 12 °C). We also include many samples from shallow lakes like those commonly studied in mid-to-high latitudes. We detect correlations of brGDGT distributions to elevation, related air temperatures, and water column temperatures, but at our sites, we find that air temperatures (either MAAT or JJAS) alone cannot explain the variations in the MBT'_{5Me} index; therefore, existing lacustrine brGDGT calibrations to MAAT [Russell et al., 2018] or to growing season air temperatures [Dang et. al., 2018] do not work well at our sites (Table 1).

Instead, our results emphasize linkages to warm season temperatures and water temperatures at depth within our study lakes (Fig. 6) suggesting in situ production. The relationships appear consistent with those of Cao et al. [2020], who proposed that brGDGT distributions track mean annual lake water temperatures, but that warm-season air temperatures strongly control these values in mid- and high-latitudes lakes. Their lake water temperature model for mid-latitudes suggest that winter ice cover decouples lake water temperatures from air temperatures as water temperatures remain constant at ~4 °C even though air temperatures drop far below 0 °C. In contrast, the model shows that lake water temperatures during the ice-free season closely track air temperatures and therefore, the mean annual lake water temperatures are biased towards the warm season. Since MAAT and JJAS at our sites are significantly correlated, we do not have statistical power to distinguish seasonality, but our results affirm a strong relationship to water temperatures (Table 2). The Cao et al., [2020] lake water temperature model could explain the strong correlation we find between the brGDGT distributions and lake water temperatures during the summer. If so, brGDGT distributions may change both as the length and maximum warmth of the ice-free season changes and some differences between the brGDGT- and pollen-inferred temperature histories at LPR may have resulted from such effects.

For the small and shallow lakes from our geographically confined study area, a relationship to water depth is also apparent and appears to modulate the temperature response (Figures 3-6). Below, we consider the source of this influence before evaluating our Bayesian model for inferred JJAS.

4.2 Influence of water depth

The distribution of lacustrine brGDGTs in sub-alpine environments of mid-latitude North America appears sensitive to both water depth and summer air temperatures (Fig. 6). The water depth is particularly significant where water depth decreases below 3 m (Fig. 6). Water depth influences both the fractional abundances (Fig. 2) and the MBT'$_{5Me}$ index (Fig. 3) with different relationships to temperature apparent in shallow (<3m) versus deep lakes (>3m) (Fig. 6). At a given elevation (and JJAS), shallow lakes exhibit higher fractional abundances of tetra-methylated compounds than deep lakes, which exhibit high abundances of hexa-methylated compounds (Fig. 2). Consequently, the MBT'$_{5Me}$ index decreases with increasing water depth and helps to explain the scatter in the relationships of JJAS (varying across elevations in Fig. 3) to individual groups of brGDGTs (Fig. 4) or the MBT'$_{5Me}$ index (Fig. 6). The MBT'$_{5Me}$ index exhibits similar negative relationships to water depth across sites (Fig. 3) and among samples from different water depths within individual lakes (Fig. 5). The consistency suggests localized influences on the suite of compounds whether through in-situ production or differences in delivery of terrestrial compounds. However, the differences with depth within individual lakes clarify that the effect is not related to length of the ice-free season nor some other factor intrinsic to shallow versus deep lakes.

Our results differ from those of Dang et al., [2018], who found no relationship between water depth and the MBT'$_{5Me}$ index, even though their study includes sites with similar water depths. This dissimilarity could be due to the fact that the sites studied by Dang et al., [2018] span a wide range of MAATs (-0.2 to 17.2 °C), which may mask the relationship between water depth and the MBT'$_{5Me}$ index because water column temperatures are a function of both water depth and air temperatures. In contrast, our sites span a relatively small range of MAATs (-0.8 to 2.6 °C) and JJAS (8.2 to 12 °C), but a relatively broad range of water depths (0.5-25 m) and T_{BOT} (4.2 to 20.1 °C), which allowed us to examine the effect of water depth on lacustrine brGDGT distributions. We also have a large proportion of samples from <3 m water depth. Additionally, the samples examined by Dang et al., [2018] have a lower fractional abundance of compound IIIa (μ =0.06, σ =0.02) than our (μ=0.26, σ=0.09) or than Russell et all., [2018] (μ=0.16, σ=0.16). The difference could result in different water depth-MBT'$_{5Me}$ relationships. Compound IIIa can weigh heavily on the MBT'$_{5Me}$ index and exhibits a strong water-depth signature (Fig. 2). We speculate that differences in bacterial communities or different environmental conditions such as salinity or high alkalinity could have caused the distinct fractional abundance distributions observed by Dang et al., [2018].

As small and shallow waterbodies dominate terrestrial environments at a global scale [Downing et al., 2006], the potential influence of lake depth on brGDGT distributions in these settings needs to be considered. Similar findings were also reported at a relatively shallow (10m deep) Gonghai Lake situated in the mid-latitudes of China where the methylation index decreases with water depth in suspended particulate matter samples (SPM) as well as in the sediments [Cao et al., 2020]. Furthermore, Cao et al. [2020] also reported an increase in the brGDGT content with increasing water depth and hypothesized that brGDGTs are likely being produced in situ, at depth in the water column. Our data also suggests that depth plays a more important role in shallow lakes and that the influence of depth on brGDGTs distributions weakens as water depth increases (Fig. 3).

We find no significant correlations between pH and the CBT' index or individual brGDGT compounds except for compound IIIa, which is significantly correlated with pH_{BOT}. Since compound IIIa is corelated to other environmental variables such as water depth, DO, T_{BOT} and MAAT, we cannot tease apart the influence of pH_{BOT} on brGDGT distributions. However, we note that other studies have found pH to have a relatively weak influence on lacustrine brGDGT distributions [Tierney et al., 2010; Loomis et al., 2014b; Russell et al., 2018].

4.3 Examining the relationship to water temperatures

At our sites, different JJAS-MBT'$_{5Me}$ relationships for lakes of different depths converge to a single relationship once T_{BOT} is considered (Fig. 6), which is a function of both lake water depth and air temperatures during the summer. During summer months, the shallow lakes are well mixed and exhibit small differences between top and bottom water temperatures (average $\Delta T = 0.2$ °C); bottom water temperatures reach temperatures as high as 20.1 °C because the whole body of well mixed waters interacts with the atmosphere. In contrast, bottom waters in deep lakes remain cool below the thermocline. The difference in mixing explains the larger range of lake bottom temperatures (4.2-20.1 °C) compared to the associated MAATs at the same sites (-0.8 to 2.2 °C) or JJAS temperatures (8.2 to 12 °C) and helps to explain the range of fractional abundances and MBT'$_{5Me}$ values (Fig. 6).

T_{BOT} exhibits the strongest relationships to both fractional abundance of all grouped compounds (Fig. 4) and to the MBT'$_{5Me}$ index (Fig. 6). The result could suggest that brGDGTs are preferentially synthesized in situ by bacteria at depth in the water column. However, multiple alternative hypotheses could explain the strong MBT'$_{5Me}$ relationship to T_{BOT}: bacteria may produce brGDGTs (1) only at depth in the water column, 2) across the full range of different temperatures and redox conditions in the complete water column, providing an integrated signal correlated with the range of T_{BOT}, including preferential production of certain compounds in different portions of the water column (e.g., hexa-methylated compounds in the hypolimnion), (3) in lake sediments, or (4) in situ, but the compounds mix in shallow water near-shore with those washed in from adjacent soils.

The various correlations within our dataset can help to evaluate the different hypotheses. For example, because average water column temperatures strongly correlate with T_{BOT}, brGDGT production throughout the water column could be tracking an integrated lake water column temperature signal. The grouped fractional abundances display the strongest correlations to T_{BOT} (Fig. 4), but the grouped tetra-methylated compounds are also significantly correlated to T_{SURF} (Spearman's r=0.68, p=0.003). The correlation between the tetra-methylated compounds and T_{SURF} could be the result of the correlation between T_{BOT} and T_{SURF}, but some fraction of the tetra-methylated compounds may be produced in surface waters. We, therefore, cannot attribute the range of brGDGT distributions at our sites solely to brGDGT production in bottom waters. This observation agrees with previous sediment trap studies that show that even though brGDGT concentrations are higher at depth in the water column than in the surface waters during thermal stratification, brGDGT production takes place throughout the water column [Loomis et al., 2014b; Buckles et al., 2014b; Miller et al., 2018]. Our correlations might be misleading, however, because single measurements of T_{BOT} may be more representative of average lake conditions during the summer than the highly variable T_{SURF}.

Additional factors other than temperature may also drive production at depth in the water column. Bacteria synthesizing hexa-methylated compounds could prefer the cool environments of bottom waters for reasons other than temperature and therefore produce patterns in the MBT'$_{5Me}$ index associated with bottom water temperatures. Weber et al. [2018] showed that different redox conditions favor the production of different individual compounds and that the concentration of compound IIIa increases below the redox zone (in the hypolimnion). However, many of our lakes are well mixed. Measured DO at 16 of our lakes suggests that most of these lakes are well oxygenated throughout the water column as bottom water anoxia was found only in four of the lakes (Supplementary Table 1). Moreover, the fractional abundance of hexa-methylated compounds and the MBT'$_{5Me}$ index suggest a weaker relationship to DO_{BOT} than to T_{BOT}. Multiple regression indicates no statistically significant linear dependence of the MBT'$_{5Me}$ index on DO_{BOT} when both DO_{BOT} and T_{BOT} are included in the model. Since anoxia was not found in all 16 lakes where DO was measured and, DO is not the best explanatory variable for compound IIIa, we speculate that, at our sites, compound IIIa is not being produced solely in anoxic waters. Instead, the decrease in the MBT'$_{5Me}$ index with increasing water depth (associated with high abundances of compound IIIa) suggests that bacteria living below the thermocline or in deep waters are producing more hexa-methylated compounds due to a decrease in water column temperatures and not due to anoxic waters. We cannot exclude the possibility that either some or all of the compounds are also being produced in the sediments [Tierney et al., 2012]. Even though sediment temperatures were not measured at our sites, we suspect that they would reflect T_{BOT} and would produce similar correlations to the MBT'$_{5Me}$ index. However, our dataset limits us from testing this hypothesis. Finally, the lack of soil data at our sites prohibits us from directly investigating the possibility that brGDGTs could also be washed into the lakes from adjacent soils, but the high abundance of hexa-methylated compounds, in particular compound IIIa (Fig, 2), and the decrease in the MBT'$_{5Me}$ index with depth within individual lakes (Fig. 5) suggests in situ production.

In summary, our study shows that lake depth and mixing regime are likely important factors in determining the distribution of brGDGTs in small lakes of mid-latitude North America and that MAAT alone cannot explain the variation in the MBT'$_{5Me}$ index. Instead, brGDGTs at our sites are likely produced in situ and therefore are sensitive to water column temperatures during the summer. Consequently, brGDGTs may be able to be used, especially with water depth information for each sample, to infer JJAS.

4.4 MBT'$_{5Me}$ calibration to temperature

We can regress T_{BOT} to the MBT'$_{5Me}$ index and reconstruct past T_{BOT} (Fig. 7,9), but for paleo-applications, T_{BOT} reconstructions and water depth histories need to be interpreted in tandem as water-depth changes can influence T_{BOT}. In many small lakes, lake-level changes are not inconsequential, even where they only result from sediment infilling (e.g., accumulation of 4.5 m of sediment in 5.7 m of water today at LPR, Fig. 9d). Therefore, calibration to JJAS, which accounts for changes in water depth, may be more useful for understanding past climate changes. Our Bayesian model shows that, if water depth is known, the MBT'$_{5Me}$ index can be used to infer JJAS (Figures 8). We found no trends in the model residuals for JJAS and log-transformed water depth (Fig. 8b,c), which suggests that all deterministic components were captured well by our model.

The challenge remains that lake bottom temperatures depend on air temperatures, but also on factors such as lake size, depth, mixing regime, depth of groundwater discharge, and lake morphometry [Almendinger et al., 1990, Rosenberry and LaBaugh 2008]. Rocky Mountain lakes such as those we studied experience lake-specific seasonal temperature trends [Liefert et al., 2018]. Strength of diurnal temperature fluctuations, maximum and minimum summer temperatures, and the magnitude of seasonal temperature changes vary even among lakes of similar size, depth, and location within the watershed. Lake volume can cause substantial differences in seasonal thermal inertia, which depresses maximum water temperatures in large lakes [Liefert et al., 2018]. Groundwater discharge, which has a fairly constant temperature, may also decrease summer lake water temperatures, but varies between lakes and can vary over time altering lake sensitivity to air temperatures [Lee, 1985; Rautio and Korkka-Niemi, 2011; Rosenberry and LaBaugh, 2008]. Because groundwater fluxes in lakes can vary on seasonal and longer time scales [Winter, 1976; Hood et al., 2006] and because thermal stratification isolates the lower portions of the water column, shallow lakes without strong groundwater connections may respond most directly to changes in air temperature through time.

Lake-level fluctuations may affect bottom water temperatures in such lakes by influencing the penetration of solar radiation and the degree of mixing, but this effect is not well expressed in many small sub-alpine lakes because the well-mixed water column quickly equilibrates with the atmosphere and observations show limited influence of even >90% reduction in lake volume [Liefert et al., 2018]. The combination of different effects indicates, however, that differences may arise between the inferred lake water temperatures and regional air temperatures, particularly in deep stratified lakes, and need to be considered when interpreting either T_{BOT} or JJAS reconstructions [Dee et al., 2018].

4.5 Temperature reconstructions from Lower Paintrock Lake, WY

Our brGDGT-based summer air temperature reconstruction from LPR shows Holocene temperatures broadly consistent with the pollen-inferred JJAS reconstruction (Fig. 9c) and other summer temperature reconstructions from the central Rocky Mountains and mid-latitude North America [Whitlock and Bartlein 1993; Shuman 2012; Shuman and Marsicek, 2016]. The air temperature trends inferred from both brGDGTs and fossil pollen agree with expected climatic drivers, such as regional warming coincident with the waning regional influence of the Laurentide Ice Sheet (LIS) and subsequent regional cooling driven by declining summer insolation (Fig. 9a). Early in the Holocene when the area and influence of the LIS retained >60% of its LGM extent and continued to exert a large influence on regional climates, summer temperatures were low even though summer insolation exceeded modern. The albedo, topographic, and meltwater effects of the LIS likely kept the northern mid-latitudes cool [Alder et al., 2015]. Temperatures rose steadily as the area and height of LIS declined. As a result, peak Holocene summer air temperatures were only achieved at LPR after ca. 9 ka.

Both the brGDGT- and pollen-based reconstructions detect significantly higher than modern temperatures during two maxima between ca. 9-5.5 ka (Fig. 9c). The inferred brGDGT summer air temperature maxima of 16.5 °C at 7.5 ka agrees with the timing of the pollen-inferred maxima of 13.3°C at 7.9 ka. Sub-alpine Wyoming lakes like LPR can reach their maximum summer temperatures in August or September, even though air temperatures peak earlier in the summer [Musselman 1994], despite the potential to bias the different reconstructions, the brGDGT-based and pollen-based JJAS trends appear consistent with each other.

Our model included the effects of the water-depth changes at LPR inferred by accounting for >4.5 m of sediment deposition during the past 14 kyrs (Fig. 9). In other cases, lake-depth history can be reconstructed using multiple sediment cores to capture common stratigraphic signals produced by lake-level changes [Digerfeldt, 1986; Pribyl and Shuman, 2014]. Because LPR remained >5.8 m deep during the Holocene, and the water-depth effect is greatest below 3 m (Fig. 3), water-depth changes had only a minimal influence on the JJAS reconstruction relative to the T_{BOT} reconstruction (Fig. 9). The trends do not differ meaningfully, except in absolute temperature, whether we use the model for T_{BOT} or JJAS (or MAAT). However, the range of temperatures for JJAS and T_{BOT} are different due to the larger range of T_{BOT} compared to the range of JJAS observed at our sites.

Unlike the pollen-inferred JJAS, the brGDGT-based temperatures inferred from the core-top samples fall 1.8 °C below even late-Pleistocene temperatures and represent the most enigmatic portion of the record (Fig. 9c). The trends and magnitude of changes in the brGDGT- and pollen-inferred reconstructions appear consistent, but the offsets in the absolute temperature might be consistent with a "cold bias" in the surface samples and calibration dataset. If so, downcore samples may contain a distribution of brGDGTs representative of a warmer environment in the calibration samples that occurred at LPR during the Holocene: a "cold bias" in surface samples would accurately correlate with modern temperature, but result in a "warm bias" in the reconstruction (i.e., greater fractional abundances of tetra- and penta-methylated compounds and fewer hexa-methylated compounds than expected from surface samples).

The "cold bias" has also been observed in other modern sediment samples [Tierney et al., 2012, Miller et al., 2018]. Possible explanations for the "cold bias" include diagenetic effects on the hexa-methylated compounds or a shift from an oxic lake environment to an anoxic lake environment [Tierney et al., 2012, Weber et al., 2018]. Diagenetic effects on the hexa-methylated compounds would decrease their abundances in older sediments resulting in increased MBT'_{5Me} values down-core. However, no evidence demonstrates different diagenetic effects on compound IIIa relative to other brGDGTs [He et al., 2012]. Although the latter would be surprising here given the history of lake shallowing (Fig. 9d), changes in the seasonal duration or thickness of lake ice cover could be important.

Another possible explanation for the downcore change would be that brGDGTs are produced in the surface sediments in addition to the water column [Tierney and Russell, 2009, 2010; Bechtel et al., 2010; Zhu et al., 2011; Loomis et al., 2012; Schoon et al., 2013; Zell et al., 2013, Miller et al., 2018, Martínez-Sosa and Tierney 2019]. High microbial activity has been shown to extend 10-15 cm into the sediments before declining substantially as energy and oxygen decline [Wurzbacher et al., 2017]. If so, brGDGTs in surface sediments could be biased towards cooler conditions of the sediment-water interface. Overall, some variations in brGDGT abundances may reflect relative changes among different sources whether they are in the water column, watershed or sediments themselves.

Based on the difference in brGDGT- reconstructed JJAS between modern sediment samples and the down core sample at ~1 ka (Fig. 9c), our Holocene summer air temperature reconstruction would be offset by +1.9 °C. The offset agrees closely (within 0.5 °C) with the difference between brGDGT- and pollen inferred JJAS in the core top samples (Δ=2.4 °C). More efforts are needed to understand the presence of the "cold bias" in sediment core-tops and future studies could test the existing hypotheses for its occurrence by either: (i) experimentally test the degradation of compound IIIa and identify possible degradation products which could either be isomerization or individual breakdown compounds; or, (ii) use high-resolution sampling of the top of sediment cores to identify where the concentration of compound IIIa attenuates. Moreover, oxic-anoxic environments should be further investigated to better understand the influence of oxygen concentrations on the production of individual brGDGT compounds.

5. Conclusion

Our study demonstrates that both temperatures and lake water depth influence the relative distributions of 5- and 6-methyl brGDGTs in sub-alpine lakes in mid-latitude North America. Most likely, the influence of depth represents the responsiveness of bacterial lipid composition to changes in water column temperatures, which are a function of both water depth and air temperatures at our sites. The MBT'_{5Me} index correlates well with T_{BOT}, which depends on both air temperatures and water depths, and likely indicates in situ production of brGDGTs within the lake. We show that if water depth is constrained by independent evidence such as sedimentation rate constraints or lake level reconstructions, past air temperatures can be inferred. Our brGDGT-based air temperature reconstruction over the last 14 ka from LPR shows trends consistent with those inferred from fossil pollen and with the known climate forcing for the region including changes in insolation and ice sheet area. Consequently, brGDGTs show promise as a useful paleothermometer at mid-latitude, high-elevation, shallow lakes.

Acknowledgements

We thank Dr. James Russell and an anonymous reviewer for providing helpful comments that greatly improved our manuscript. We thank P. Murphy for lab analyses and J. Calder, A. Flaim, M. Parish and D. Liefert for assistance with sample collection. This work was supported by the Microbial Ecology Collaborative Project at the University of Wyoming through the National Science Foundation grant EPS-1655726. J. Tierney acknowledges funding support from the National Science Foundation grant EAR-1603674.

Data associated with this article is available through the Mountain Scholar database at http://dx.doi.org/10.15786/20.500.11919/7164.

References

Alder, J.R. and Hostetler, S.W., 2015. Global climate simulations at 3000-year intervals for the last 21 000 years with the GENMOM coupled atmosphere-ocean model. Climate of the Past 11, pp. 449–471.

Almendinger, J.E., 1990. Groundwater control of closed-basin lake levels under steady-state conditions. Journal of Hydrology 112, pp. 293-318.

Bechtel, A., Smittenberg, R.H., Bernasconi, S.M. and Schubert, C.J., 2010. Distribution of branched and isoprenoid tetraether lipids in an oligotrophic and a eutrophic Swiss lake: insights into sources and GDGT-based proxies. Organic Geochemistry 41, pp. 822-832.

Berger A. and Loutre M.F., 1991. Insolation values for the climate of the last 10 million years. Quaternary Sciences Review 10, pp. 297-317.

Buckles, L.K., Weijers, J.W., Verschuren, D. and Damsté, J.S.S., 2014b. Sources of core and intact branched tetraether membrane lipids in the lacustrine environment: Anatomy of Lake Challa and its catchment, equatorial East Africa. Geochimica et Cosmochimica Acta 140, pp. 106-126.

Buckles, L.K., Weijers, J.W.H., Tran, X.M., Waldron, S. and Sinninghe Damsté, J.S., 2014a. Provenance of tetraether membrane lipids in a large temperate lake (Loch Lomond, UK): implications for glycerol dialkyl glycerol tetraether (GDGT)-based palaeothermometry. Biogeosciences 11, pp. 5539-5563.

Calder, W.J., Parker, D., Stopka, C.J., Jiménez-Moreno, G. and Shuman, B.N., 2015. Medieval warming initiated exceptionally large wildfire outbreaks in the Rocky Mountains. Proceedings of the National Academy of Sciences 112, pp. 13261-13266.

Cao, J., Rao, Z., Shi, F. and Jia, G., 2020. Ice formation on lake surfaces in winter causes warm-season bias of lacustrine brGDGT temperature estimates. Biogeosciences 17, pp. 2521-2536.

Crampton-Flood, E.D., Tierney, J.E., Peterse, F., Kirkels, F.M. and Damsté, J.S.S., 2020. BayMBT: A Bayesian calibration model for branched glycerol dialkyl glycerol tetraethers in soils and peats. Geochimica et Cosmochimica Acta 268, pp. 142-159.

Dang, X., Ding, W., Yang, H., Pancost, R.D., Naafs, B.D.A., Xue, J., Lin, X., Lu, J. and Xie, S., 2018. Different temperature dependence of the bacterial brGDGT isomers in 35 Chinese lake sediments compared to that in soils. Organic Geochemistry 119, pp. 72-79.

Dee, S.G., Russell, J.M., Morrill, C., Chen, Z. and Neary, A., 2018. PRYSM v2. 0: A proxy system model for lacustrine archives. Paleoceanography and Paleoclimatology 33, pp. 1250-1269.

De Jonge, C., Stadnitskaia, A., Hopmans, E.C., Cherkashov, G., Fedotov, A. and Damsté, J.S.S., 2014b. In situ produced branched glycerol dialkyl glycerol tetraethers in suspended particulate matter from the Yenisei River, Eastern Siberia. Geochimica et Cosmochimica Acta 125, pp. 476-491.

De Jonge, C., Hopmans, E.C., Zell, C.I., Kim, J.H., Schouten, S. and Damsté, J.S.S., 2014a. Occurrence and abundance of 6-methyl branched glycerol dialkyl glycerol tetraethers in soils: Implications for palaeoclimate reconstruction. Geochimica et Cosmochimica Acta 141, pp. 97-112.

De Jonge, C., Hopmans, E.C., Stadnitskaia, A., Rijpstra, W.I.C., Hofland, R., Tegelaar, E. and Damsté, J.S.S., 2013. Identification of novel penta-and hexamethylated branched glycerol dialkyl glycerol tetraethers in peat using

HPLC–MS2, GC–MS and GC–SMB-MS. Organic Geochemistry 54, pp. 78-82.

Digerfeldt, G., 1986. Studies on Past Lake-Level Fluctuations. Handbook of Holocene Palaeoecology and Palaeohydrology, pp. 127–143. John Wiley and Sons, New York.

Dirghangi, S.S., Pagani, M., Hren, M.T. and Tipple, B.J., 2013. Distribution of glycerol dialkyl glycerol tetraethers in soils from two environmental transects in the USA. Organic Geochemistry 59, pp. 49-60.

Downing, J.A., Prairie, Y.T., Cole, J.J., Duarte, C.M., Tranvik, L.J., Striegl, R.G., McDowell, W.H., Kortelainen, P., Caraco, N.F., Melack, J.M. and Middelburg, J.J., 2006. The global abundance and size distribution of lakes, ponds, and impoundments. Limnology and Oceanography 51, pp. 2388-2397.

Dyke, A.S., 2004. An outline of North American deglaciation with emphasis on central and northern Canada. Developments in Quaternary Sciences 2, pp. 373-424.

Feng, X., Zhao, C., D'Andrea, W.J., Liang, J., Zhou, A. and Shen, J., 2019. Temperature fluctuations during the Common Era in subtropical southwestern China inferred from brGDGTs in a remote alpine lake. Earth and Planetary Science Letters 510, pp. 26-36.

Fleming, L.E. and Tierney, J.E., 2016. An automated method for the determination of the TEX86 and U37K′ paleotemperature indices. Organic Geochemistry 92, pp. 84-91.

Green, G.N. and Drouillard, P.H., 1994. The digital geologic map of Wyoming in ARC/INFO format. US Department of the Interior, US Geological Survey.

He, L., Zhang, C.L., Dong, H., Fang, B. and Wang, G., 2012. Distribution of glycerol dialkyl glycerol tetraethers in Tibetan hot springs. Geoscience Frontiers 3, pp. 289-300.

Hood, J.L., Roy, J.W. and Hayashi, M., 2006. Importance of groundwater in the water balance of an alpine headwater lake. Geophysical Research Letters 33, pp. 1-5.

Hopmans, E.C., Schouten, S. and Damsté, J.S.S., 2016. The effect of improved chromatography on GDGT-based palaeoproxies. Organic Geochemistry 93, pp. 1-6.

Hopmans, E.C., Weijers, J.W., Schefuß, E., Herfort, L., Damsté, J.S.S. and Schouten, S., 2004. A novel proxy for terrestrial organic matter in sediments based on branched and isoprenoid tetraether lipids. Earth and Planetary Science Letters 224, pp. 107-116.

Huguet, C., Hopmans, E.C., Febo-Ayala, W., Thompson, D.H., Damsté, J.S.S. and Schouten, S., 2006. An improved method to determine the absolute abundance of glycerol dibiphytanyl glycerol tetraether lipids. Organic Geochemistry 37, pp. 1036-1041.

Lee, L.Y.W., Chen, J.C. and Nelson, R.A., 1985. Liquid-solid contact measurements using a surface thermocouple temperature probe in atmospheric pool boiling water. International Journal of Heat and Mass Transfer 28, pp. 1415-1423.

Leng, M.J. and Marshall, J.D., 2004. Palaeoclimate interpretation of stable isotope data from lake sediment archives. Quaternary Science Reviews 23, pp. 811-831.

Liefert, D.T., Shuman, B.N., Parsekian, A.D. and Mercer, J.J., 2018. Why are some rocky mountain lakes ephemeral? Water Resources Research 54, pp. 5245-5263.

Loomis, S.E., Russell, J.M. and Lamb, H.F., 2015. Northeast African temperature variability since the Late Pleistocene. Palaeogeography, Palaeoclimatology, Palaeoecology 423, pp.80-90.

Loomis, S.E., Russell, J.M., Eggermont, H., Verschuren, D. and Damsté, J.S.S., 2014b. Effects of temperature, pH and nutrient concentration on branched GDGT distributions in East African lakes: Implications for paleoenvironmental reconstruction. Organic Geochemistry 66, pp.25-37.

Loomis, S.E., Russell, J.M., Heureux, A.M., D'Andrea, W.J. and Damsté, J.S.S., 2014a. Seasonal variability of branched glycerol dialkyl glycerol tetraethers (brGDGTs) in a temperate lake system. Geochimica et Cosmochimica Acta 144, pp. 173-187.

Loomis, S.E., Russell, J.M., Ladd, B., Street-Perrott, F.A. and Damsté, J.S.S., 2012. Calibration and application of the branched GDGT temperature proxy on East African lake sediments. Earth and Planetary Science Letters 357, pp. 277-288.

Marsicek, J., Shuman, B.N., Bartlein, P.J., Shafer, S.L. and Brewer, S., 2018. Reconciling divergent trends and millennial variations in Holocene temperatures. Nature 554, pp. 92-96.

Martínez-Sosa, P. and Tierney, J.E., 2019. Lacustrine brGDGT response to microcosm and mesocosm incubations. Organic Geochemistry 127, pp. 12-22.

MATLAB. 2019. version 9.6.0.1214997 (R2019a) Update 6. Natick, Massachusetts: The MathWorks Inc.

Miller, D.R., Habicht, M.H., Keisling, B.A., Castañeda, I.S. and Bradley, R.S., 2018. A 900-year New England temperature reconstruction from in situ seasonally produced branched glycerol dialkyl glycerol tetraethers (brGDGTs). Climate of the Past 14, pp. 1653–1667.

Minckley, T. A., Shriver, R. K., & Shuman, B. 2012. Resilience and regime change in a southern Rocky Mountain ecosystem during the past 17 000 years. Ecological Monographs 82, pp. 49-68.

Musselman, R.C., 1994. The glacier lakes ecosystem experiments site. US Department of Agriculture, Forest Service, Rocky Mountain Forest and Range Experiment Station.

Naafs, B.D.A., Inglis, G.N., Zheng, Y., Amesbury, M.J., Biester, H., Bindler, R., Blewett, J., Burrows, M.A., Del Castillo Torres, D., Chambers, F.M. and Cohen, A.D., 2017b. Introducing global peat-specific temperature and pH calibrations based on brGDGT bacterial lipids. Geochimica et Cosmochimica Acta 208, pp. 285-301.

Naafs, B.D.A., Gallego-Sala, A.V., Inglis, G.N. and Pancost, R.D., 2017a. Refining the global branched glycerol dialkyl glycerol tetraether (brGDGT) soil temperature calibration. Organic Geochemistry 106, pp. 48-56.

Ning, D., Zhang, E., Shulmeister, J., Chang, J., Sun, W. and Ni, Z., 2019. Holocene mean annual air temperature (MAAT) reconstruction based on branched glycerol dialkyl glycerol tetraethers from Lake Ximenglongtan, southwestern China. Organic Geochemistry 133, pp. 65-76.

Parish, M.C., Calder, W.J. and Shuman, B.N., 2020. Millennial-scale increase in winter precipitation in the southern Rocky Mountains during the Common Era. Quaternary Research 94, pp. 1-13.

Parnell, A.C., Haslett, J., Allen, J.R., Buck, C.E. and Huntley, B., 2008. A flexible approach to assessing synchroneity of past events using Bayesian reconstructions of sedimentation history. Quaternary Science Reviews 27, pp. 1872-1885.

Peterse, F., van der Meer, J., Schouten, S., Weijers, J.W., Fierer, N., Jackson, R.B., Kim, J.H. and Damsté, J.S.S., 2012. Revised calibration of the MBT–CBT paleotemperature proxy based on branched tetraether membrane lipids in surface soils. Geochimica et Cosmochimica Acta 96, pp. 215-229.

Peterse, F., Kim, J.H., Schouten, S., Kristensen, D.K., Koç, N. and Damsté, J.S.S., 2009. Constraints on the application of the MBT/CBT palaeothermometer at high latitude environments (Svalbard, Norway). Organic Geochemistry 40, pp. 692-699.

Polanco-Martinez, J.M., Medina-Elizalde, M.A., Goni, M.F.S. and Mudelsee, M., 2019. BINCOR: An R package for Estimating the Correlation between Two Unevenly Spaced Time Series. The R Journal 11, pp. 1-14.

Pribyl, P. and Shuman, B.N., 2014. A computational approach to Quaternary lake-level reconstruction applied in the central Rocky Mountains, Wyoming, USA. Quaternary Research 82, pp. 249-259.

PRISM Climate Group, Oregon State University, http://prism.oregonstate.edu, created June 2018.

R Core Team, 2018. R: A language and environment for statistical computing. R Foundation for Statistical Computing, Vienna, Austria. URL https://www.R-project.org/.

Rautio, A. and Korkka-Niemi, K., 2011. Characterization of groundwater–lake water interactions at Pyhäjärvi, a lake in SW Finland. Boreal Environment Research 16: pp. 363–380.

Rosenberry, D. O., & LaBaugh, J. W., 2008. Field techniques for estimating water fluxes between surface water and ground. USGS, Reston, Virginia.

Russell, J.M., Hopmans, E.C., Loomis, S.E., Liang, J. and Damsté, J.S.S., 2018. Distributions of 5-and 6-methyl branched glycerol dialkyl glycerol tetraethers (brGDGTs) in East African lake sediment: Effects of temperature, pH, and new lacustrine paleotemperature calibrations. Organic Geochemistry 117, pp. 56-69.

Rust, R.A. and Minckley, T.A., 2020. Fire and hydrologically mediated diversity change in subalpine forests through the Holocene. Journal of Vegetation Science 31, pp. 380-391.

Schoon, P.L., de Kluijver, A., Middelburg, J.J., Downing, J.A., Damsté, J.S.S. and Schouten, S., 2013. Influence of lake water pH and alkalinity on the distribution of core and intact polar branched glycerol dialkyl glycerol tetraethers (GDGTs) in lakes. Organic Geochemistry 60, pp. 72-82.

Schouten, S., Hopmans, E.C., Pancost, R.D. and Damsté, J.S.S., 2000. Widespread occurrence of structurally diverse tetraether membrane lipids: evidence for the ubiquitous presence of low-temperature relatives of hyperthermophiles. Proceedings of the National Academy of Sciences 97, pp. 14421-14426.

Sinninghe Damsté, J.S., 2016. Spatial heterogeneity of sources of branched tetraethers in shelf systems: The geochemistry of tetraethers in the Berau River delta (Kalimantan, Indonesia). Geochimica et Cosmochimica Acta 186, pp. 13-31.

Sinninghe Damsté, J.S., Ossebaar, J., Abbas, B., Schouten, S. and Verschuren, D., 2009. Fluxes and distribution of tetraether lipids in an equatorial African lake: constraints on the application of the TEX86 palaeothermometer and BIT index in lacustrine settings. Geochimica et Cosmochimica Acta 73, pp. 4232-4249.

Sinninghe Damsté, J.S., Hopmans, E.C., Pancost, R.D., Schouten, S. and Geenevasen, J.A., 2000. Newly discovered non-isoprenoid glycerol dialkyl glycerol tetraether lipids in sediments. Chemical Communications 17, pp. 1683-1684.

Shuman, B.N. and Serravezza, M., 2017. Patterns of hydroclimatic change in the Rocky Mountains and surrounding regions since the last glacial maximum. Quaternary Science Reviews 173, pp. 58-77.

Shuman, B.N. and Marsicek, J., 2016. The structure of Holocene climate change in mid-latitude North America. Quaternary Science Reviews 141, pp. 38-51.

Shuman, B., 2012. Recent Wyoming temperature trends, their drivers, and impacts in a 14,000-year context. Climatic Change 112, pp. 429-447.

Tierney, J.E., Malevich, S.B., Gray, W., Vetter, L. and Thirumalai, K., 2019. Bayesian calibration of the Mg/Ca paleothermometer in planktic foraminifera. Paleoceanography and Paleoclimatology 34, pp. 2005-2030.

Tierney, J.E. and Tingley, M.P., 2014. A Bayesian, spatially-varying calibration model for the TEX86 proxy. Geochimica et Cosmochimica Acta 127, pp. 83-106.

Tierney, J.E., Schouten, S., Pitcher, A., Hopmans, E.C. and Damsté, J.S.S., 2012. Core and intact polar glycerol dialkyl glycerol tetraethers (GDGTs) in Sand Pond, Warwick, Rhode Island (USA): Insights into the origin of lacustrine GDGTs. Geochimica et Cosmochimica Acta 77, pp. 561-581.

Tierney, J.E., Russell, J.M., Eggermont, H., Hopmans, E.C., Verschuren, D. and Damsté, J.S., 2010. Environmental controls on branched tetraether lipid distributions in tropical East African lake sediments. Geochimica et Cosmochimica Acta 74, pp. 4902-4918.

Tierney, J.E. and Russell, J.M., 2009. Distributions of branched GDGTs in a tropical lake system: implications for lacustrine application of the MBT/CBT paleoproxy. Organic Geochemistry 40, pp. 1032-1036.

Weber, Y., Damsté, J.S.S., Zopfi, J., De Jonge, C., Gilli, A., Schubert, C.J., Lepori, F., Lehmann, M.F. and Niemann, H., 2018. Redox-dependent niche differentiation provides evidence for multiple bacterial sources of glycerol tetraether lipids in lakes. Proceedings of the National Academy of Sciences 115, pp. 10926-10931.

Weijers, J.W., Panoto, E., van Bleijswijk, J., Schouten, S., Rijpstra, W.I.C., Balk, M., Stams, A.J. and Damste, J.S.S., 2009. Constraints on the biological source (s) of the orphan branched tetraether membrane lipids. Geomicrobiology Journal 26, pp. 402-414.

Weijers, J.W., Schouten, S., van den Donker, J.C., Hopmans, E.C. and Damsté, J.S.S., 2007. Environmental controls on bacterial tetraether membrane lipid distribution in soils. Geochimica et Cosmochimica Acta 71, pp. 703-713.

Weijers, J.W., Schouten, S., Hopmans, E.C., Geenevasen, J.A., David, O.R., Coleman, J.M., Pancost, R.D. and Sinninghe Damsté, J.S., 2006. Membrane lipids of mesophilic anaerobic bacteria thriving in peats have typical archaeal traits. Environmental Microbiology 8, pp. 648-657.

Whitlock, C. and Bartlein, P.J., 1993. Spatial variations of Holocene climatic change in the Yellowstone region. Quaternary Research 39, pp. 231-238.

Winter, T.C., 1976. Numerical simulation analysis of the interaction of lakes and ground water. US Geological Survey Professional Paper 1001.

Wurzbacher, C., Fuchs, A., Attermeyer, K., Frindte, K., Grossart, H.P., Hupfer, M., Casper, P. and Monaghan, M.T., 2017. Shifts among Eukaryota, Bacteria, and Archaea define the vertical organization of a lake sediment. Microbiome 5, pp. 1-16.

Zell, C., Kim, J.H., Moreira-Turcq, P., Abril, G., Hopmans, E.C., Bonnet, M.P., Sobrinho, R.L. and Damsté, J.S.S., 2013. Disentangling the origins of branched tetraether lipids and crenarchaeol in the lower Amazon River: Implications for GDGT-based proxies. Limnology and Oceanography 58, pp. 343-353.

Zhu, C., Weijers, J.W., Wagner, T., Pan, J.M., Chen, J.F. and Pancost, R.D., 2011. Sources and distributions of tetraether lipids in surface sediments across a large river-dominated continental margin. Organic Geochemistry 42, pp. 376-386.

Figure captions:

Fig. 1. Map showing the location of 34 lakes sampled (circles and diamond) with elevation as color scale. The diamond symbol represents the location of Lower Paintrock Lake where we applied our brGDGT calibration.

Fig. 2. Boxplot showing the fractional abundances of individual brGDGTs in lake surface sediment samples from: A) all lakes - all sampling depths, n=39; B) shallow lakes (this study: sample depth <3 meters, n=17); C) deep lakes (this study: sample depth >3 meters, n=22). Box plot interpretation: lower whisker shows the lowest value, lower hinge shows the first quantile (the 25th percentile), middle hinge shows second quantile (50th percentile or the median,) upper hinge shows the third quantile (75th percentile) and the upper whisker shows the highest value.

Fig. 3. Sediment sampling depth in meters versus MBT'_{5Me} with elevation for color scale, (n=39).

Fig. 4. Grouped fractional abundances of tetra-, penta- and hexa-methylated brGDGTs (n=17) versus: A) Mean summer air temperature (JJAS); B) Summer lake surface temperature (T_{SURF}); C) Summer lake bottom temperature (T_{BOT}). Spearman's correlation coefficients (r) and associated p-values are shown in each subplot.

Fig. 5. MBT'_{5Me} values as a function of modern sediment depth at Round (open triangles), Rainbow Lake (filled circles) and Duncan Lake (filled squares) located at elevations of 3232m, 3000, and 2800 m, respectively.

Fig. 6. Relationship between the MBT'$_{5Me}$ index and: A) Mean summer air temperature (JJAS), n=39; B) Summer lake surface temperatures (T_{SURF}), n=17; C) Summer lake bottom temperatures (T_{BOT}), n=17. Diamonds represent shallow lakes (<3m) and circles represent deep lakes (>3m). Regression lines represent the relationship between the individual variables (JJAS, T_{SURF} and T_{BOT}) and the MBT'$_{5Me}$ index for: shallow lakes (red dashed line), deep lakes (blue dashed line) and all depths (black solid line).

Fig. 7. Observed T_{BOT} versus Bayesian estimated T_{BOT}. Solid line denotes the 1:1 reference line and residuals are plotted atop.

Fig. 8. A) Observed MBT'$_{5Me}$ index versus Bayesian estimated MBT'$_{5Me}$ index; B) Observed mean summer air temperatures (JJAS) versus Bayesian estimated JJAS temperatures; C) Observed ln(water depth) versus Bayesian estimated ln(water depth). Solid lines denote the 1:1 reference lines and residuals are plotted atop each scatterplot. LPR is shown in red.

Fig. 9. A) Laurentide Ice Sheet percent area (light blue shaded area) [Dyke A. 2004] and the insolation curve at 60°N (red line) [Berger and Loutre, 1991]. B) Reconstructed T_{BOT} (diamonds) at Lower Paintrock Lake, shaded grey area represents the central 50% credible interval. C) BrGDGT-based JJAS (black line) at Lower Paintrock Lake, shaded grey area represents the central 50% credible interval; pollen-based JJAS (orange line), shaded light orange area represents ±RMSE (RMSE=1.8 °C). D) The water depth history (blue dashed line) at Lower Paintrock Lake, WY. All versus calibrated kyrs before 1950.

Table 1. Site locations and environmental data

Lake	Latitude	Longitude	Elevation (m)	Maximum depth (m)	Sample water depth (m)	Summer water temperature °C		MAAT °C	JJAS °C	MBT'$_{5Me}$	MAAT °C Russell et al. 2018	MAAT °C Dang et al. 2018
						top	bottom					
Bear	40.775°N	106.631°W	3182	6	6			0.6	10.2	0.152	3.7	-5.6
Beaver	40.754°N	106.686°W	3176	5.5	5.5			0.6	10.1	0.213	5.7	-0.7
Brooklyn	41.373°N	106.249°W	3233	11.6	11.6	13.8	6.7	-0.2	8.9	0.199	5.3	-2.2
Crater	41.491°N	106.247°W	3001	19.8	16	15.2	4.3	0.9	10.2	0.176	4.5	-1.9
Duncan	44.647°N	107.447°W	2798	1.8	1.8			0.8	10	0.368	10.7	7
East Glacier	41.377°N	106.259°W	3312	7.6	6	13.4	12	-0.4	8.5	0.129	2.9	-6.4
Eileen	40.903°N	106.673°W	3168	5.7	5.7			0	9.5	0.235	6.4	0.1
Fire Box	41.442°N	106.193°W	2935	1	0.5	20.6	20.1	1.6	10.7	0.4	11.8	10.3
Fishhook	41.357°N	106.267°W	3232	1.7	1.7	13.6	13.6	0	9	0.288	8.1	6.5
Gem	40.881°N	106.734°W	3180	6.5	6.5			0.2	9.4	0.221	5.9	0.4
Highway 130	41.351°N	106.264°W	3201	1.5	0.8	14.6	14.5	0.2	9.2	0.332	9.6	9.9
Hourglass	41.350°N	106.271°W	3214	1.2	1.1	13.1	12.9	0.2	9.1	0.353	10.2	6.5
Lewis	41.359°N	106.296°W	3311	10.1	9.9	15.2	8.4	-0.6	8.5	0.201	5.4	0.4
Libby Flats	41.324°N	106.286°W	3199	1.2	0.5			0.2	9.2	0.397	11.6	13.4
Libby Flats 1	41.332°N	106.294°W	3233	0.89	0.89			0..1	9	0.341	9.9	7.1
Libby Flats 3	41.319°N	106.280°W	3200	0.49	0.49			0.1	9.1	0.38	11.1	12.5
Libby	41.354°N	106.298°W	3297	12.2	10.3	12.5	7.7	-0.6	8.5	0.159	3.9	-2.4
Little Jeep	41.353°N	106.277°W	3252	1.5	1.5			0.2	8.9	0.339	9.8	6.2
Lost	41.445°N	106.118°W	2819	1	0.6	16.2	16.1	2.2	11.3	0.342	9.9	8.6
Lower Paintrock	44.390°N	107.380°W	2814	5.8	5.8			0.6	10	0.239	6.5	3.3
Middle Rainbow	40.648°N	106.624°W	3016	5.8	5.8			1.2	10.6	0.227	6.2	2.4
Mirror Lake	41.338°N	106.320°W	3241	15.7	15.7	12.9	5.8	-0.3	8.9	0.205	5.4	-4.8
North Banner	41.415°N	106.358°W	3040	4.2	3.3	19.2	16.6	1.1	10.1	0.267	7.4	0.4
Rainbow	44.936°N	109.500°W	2959	2.5	1			0.8	8.2	0.314	9	2.9
Round	41.359°N	106.269°W	3249	1.2	1.2	15.9	13.6	0	8.9	0.256	7.1	6.1
Round Mountain	40.585°N	106.678°W	3045	3.5	3.5			1.3	10.6	0.241	6.6	0.9
Seven	40.896°N	106.681°W	3250	5.8	5.8			0	9.4	0.234	6.4	-0.8
Silver	41.309°N	106.357°W	3191	7.6	7	14.3	8.9	-0.1	9	0.179	4.6	1.4
Silver Run	41.327°N	106.237°W	3068	4.3	4.3	15.8	13.2	0.9	9.9	0.266	7.4	6.7
South Gap	41.369°N	106.299°W	3369	21.3	16.2	12.2	5.6	-0.8	8.2	0.099	2	-7.3
Stamp Mill	41.350°N	106.381°W	3039	3.9	3.9	18.6	16.2	1.1	10	0.291	8.2	3
Teal	40.583°N	106.608°W	2700	13.1	13.1			2.6	12	0.314	9	7.1
Unnamed	40.506°N	106.617°W	2797	6	6			2.1	11.7	0.29	8.2	5.1
Whale	40.556°N	106.675°W	3086	11.5	11.5			1.1	10.6	0.215	5.8	-0.2

Table 2. Pairwise correlations of environmental data. Statistically significant correlations are shown in bold.

Spearman's correlations	Elevation m	Water depth m	MAAT °C	JJAS °C	T_{SURF} °C	T_{BOT} °C	Average water temp. °C	DO_{SURF} mg/L	DO_{BOT} mg/L	pH_{SURF}
Water depth m	r=0.25 p=0.125 n=39	-	-	-	-	-	-	-	-	-
MAAT °C	**r=-0.84** **p<0.001** **n=-39**	r=-0.19 p=0.252 n=39	-	-	-	-	-	-	-	-
JJAS °C	**r=-0.62** **p<0.001** **n=39**	r=0.02 p=0.912 n=39	**r=0.75** **p<0.001** **n=39**	-	-	-	-	-	-	-
T_{SURF} °C	**r=-0.78** **p<0.001** **n=17**	**r=-0.56** **p=0.018** **n=17**	**r=0.80** **p<0.001** **n=17**	**r=0.73** **p<0.001** **n=17**	-	-	-	-	-	-
T_{BOT} °C	**r=-0.64** **p=0.005** **n=17**	**r=-0.89** **p<0.001** **n=17**	**r=0.73** **p<0.001** **n=17**	**r=0.60** **p=0.011** **n=17**	**r=0.73** **p<0.001** **n=17**	-	-	-	-	-
Average water temp. °C	**r=-0.68** **p=0.003** **n=17**	**r=-0.67** **p=0.003** **n=17**	**r=0.69** **p=0.002** **n=17**	**r=0.64** **p=0.005** **n=17**	**r=0.64** **p=0.006** **n=17**	**r=0.83** **p<0.001** **n=17**	-	-	-	-
DO_{SURF} mg/L	r=0.05 p=0.864 n=16	r=-0.13 p=0.629 n=16	r=0.03 p=0.918 n=16	r=0.02 p=0.957 n=16	r=0.19 p=0.479 n=16	r=0.16 p=0.557 n=16	r=0.10 p=0.712 n=16	-	-	-
DO_{BOT} mg/L	r=-0.36 p=0.166 n=16	**r=-0.66** **p=0.005** **n=16**	r=0.47 p=0.070 n=16	r=0.39 p=0.140 n=16	**r=0.54** **p=0.032** **n=16**	**r=0.71** **p=0.002** **n=16**	**r=0.75** **p<0.001** **n=16**	r=0.45 p=0.081 n=16	-	-
pH_{SURF}	r=-0.36 p=0.197 n=16	r=-0.27 p=0.337 n=16	r=-0.20 p=0.274 n=16	r=-0.26 p=0.351 n=16	r=-0.33 p=0.223 n=16	r=-0.33 p=0.223 n=16	r=-24 p=0.394 n=16	r=0.51 p=0.055 n=16	r=0.11 p=0.708 n=16	-
pH_{BOT}	**r=-0.52** **p=0.045** **n=16**	**r=-0.67** **p=0.006** **n=16**	**r=0.60** **p=0.018** **n=16**	**r=0.62** **p=0.014** **n=16**	r=0.43 p=0.113 n=16	**r=0.56** **p=0.031** **n=16**	**r=0.59** **p=0.022** **n=16**	r=0.34 p=0.215 n=16	**r=0.68** **p=0.005** **n=16**	r=0.34 p=0.208 n=16

Table 3. Pairwise correlations between environmental variables and the MBT'_{5Me} and CBT' indices. Statistically significant correlations are shown in bold.

Spearman's correlations	MBT'_{5Me}	CBT'
MAAT °C	**r=0.436** **p=0.006** **n=39**	r=-0.128 p=0.438 n=39
JJAS °C	r=0.208 p=0.203 n=39	r=-0.178 p=0.278 n=39
T_{BOT} °C	**r=0.790** **p<0.001** **n=17**	r=-0.159 p=0.0.541 n=17
T_{TOP} °C	**r=0.565** **p=0.018** **n=17**	r=-0.221 p=0.392 n=17
DO_{BOT} mg/L	**r=0.632** **p=0.009** n=16	r=-0.035 p=0.897 n=16
DO_{TOP} mg/L	r=0.152 p=0.575 n=16	r=-0.262 p=0.327 n=16
pH_{BOT}	**r=0.606** **p=0.017** **n=16**	r=0.298 p=0.280 n=16
pH_{TOP}	r=-0.198 p=0.478 n=16	r=0.295 p=0.286 n=16

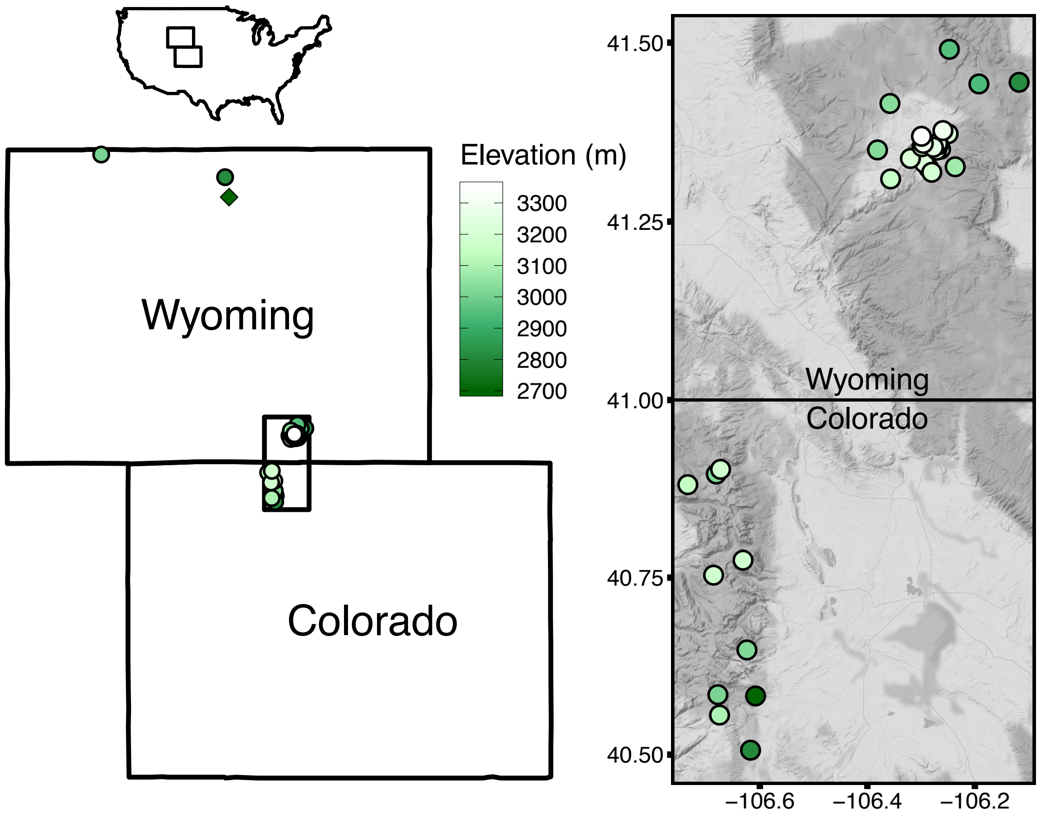

Elevation (m)
3300
3200
3100
3000
2900
2800
2700
Wyoming
Colorado
41.50
41.25
41.00
40.75
40.50
−106.6
−106.4
−106.2

Figure 1.

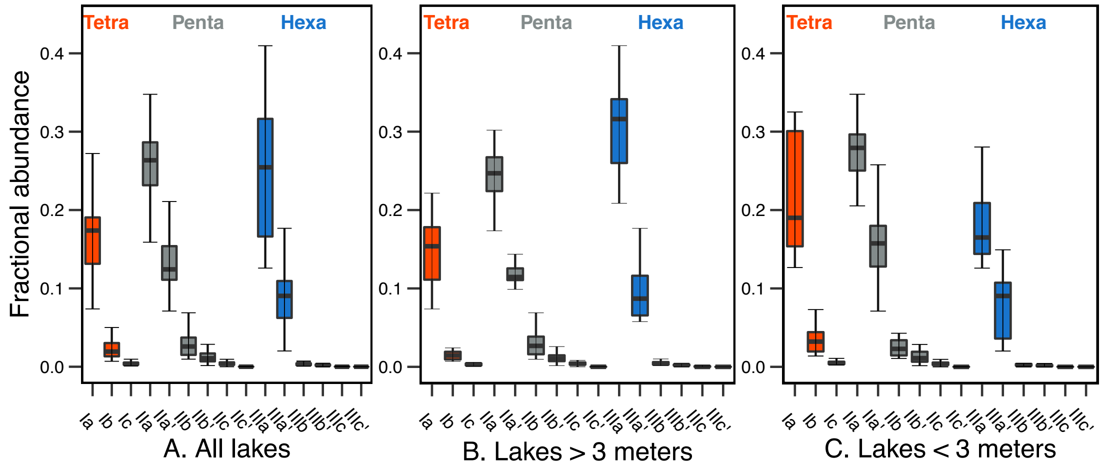

Tetra
Penta
Hexa
Fractional abundance
0.4
0.3
0.2
0.1
0.0
Ia
Ib
Ic
IIa
IIa'
IIb
IIb'
IIc
IIc'
IIIa
IIIa'
IIIb
IIIb'
IIIc
IIIc'
A. All lakes
B. Lakes > 3 meters
C. Lakes < 3 meters

Figure 2.

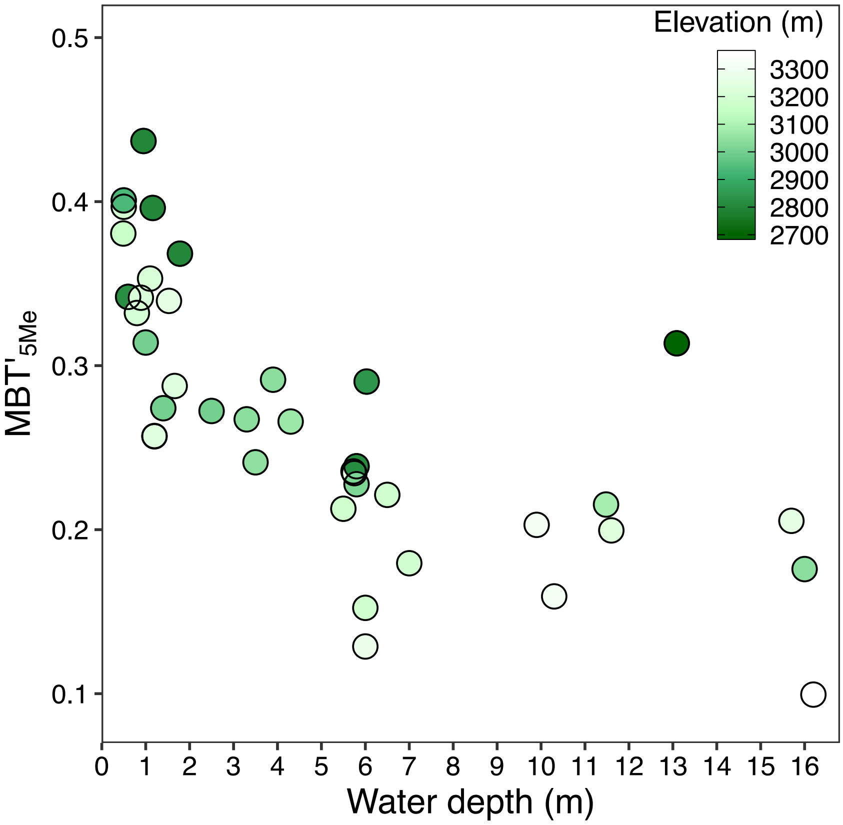

Elevation (m)
3300
3200
3100
3000
2900
2800
2700
0.5
0.4
0.3
0.2
0.1
MBT'5Me
0 1 2 3 4 5 6 7 8 9 10 11 12 13 14 15 16
Water depth (m)

Figure 3.

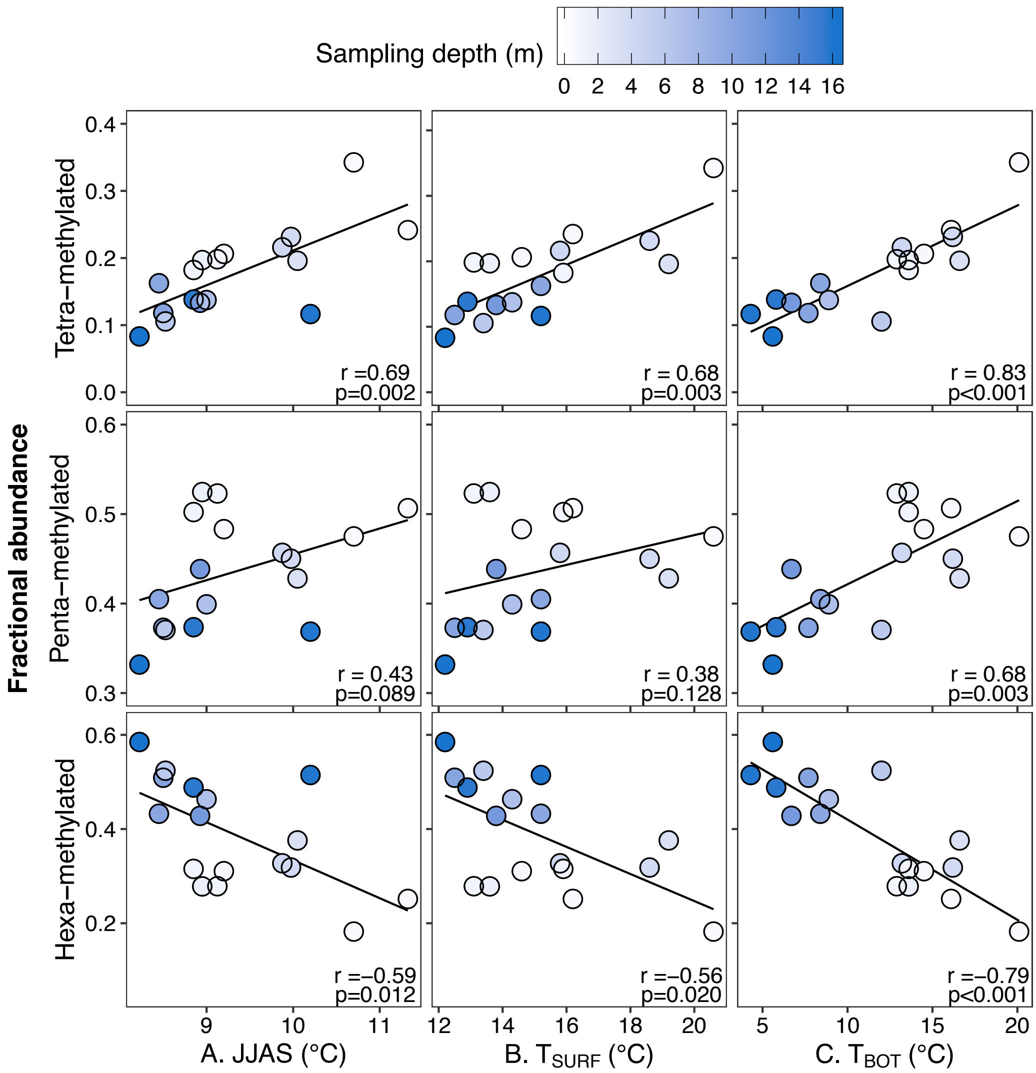

Sampling depth (m)
0 2 4 6 8 10 12 14 16
Fractional abundance
Tetra−methylated
Penta−methylated
Hexa−methylated
r =0.69
p=0.002
r = 0.68
p=0.003
r = 0.83
p<0.001
r = 0.43
p=0.089
r = 0.38
p=0.128
r = 0.68
p=0.003
r =−0.59
p=0.012
r =−0.56
p=0.020
r =−0.79
p<0.001
A. JJAS (°C)
B. T_SURF (°C)
C. T_BOT (°C)

Figure 4.

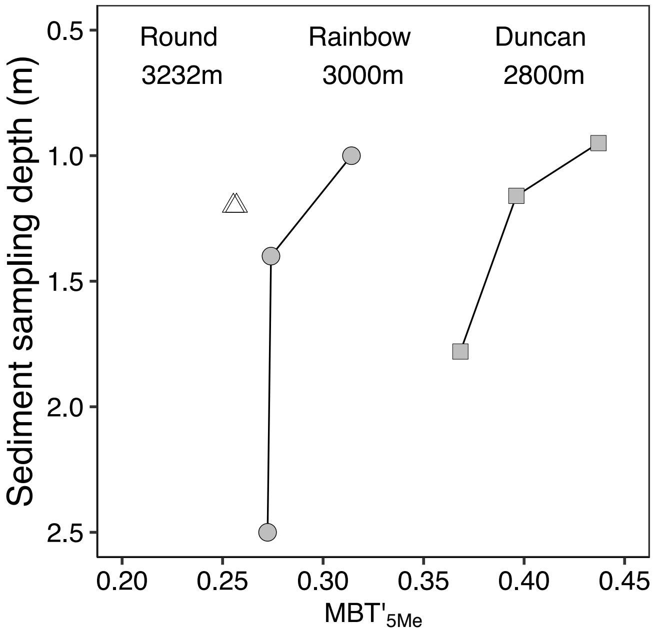
Round
3232m
Rainbow
3000m
Duncan
2800m
Sediment sampling depth (m)
0.5
1.0
1.5
2.0
2.5
0.20
0.25
0.30
0.35
0.40
0.45
MBT'5Me

Figure 5.

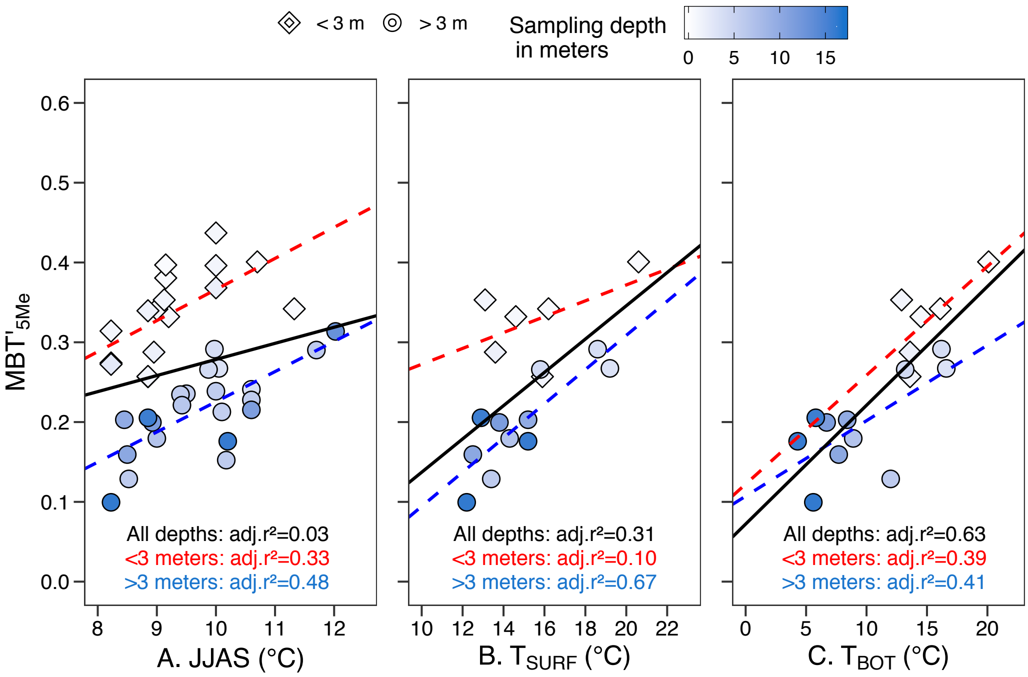

< 3 m
> 3 m
Sampling depth
in meters
0 5 10 15
MBT'5Me
0.6
0.5
0.4
0.3
0.2
0.1
0.0
All depths: adj.r²=0.03
<3 meters: adj.r²=0.33
>3 meters: adj.r²=0.48
8 9 10 11 12
A. JJAS (°C)
All depths: adj.r²=0.31
<3 meters: adj.r²=0.10
>3 meters: adj.r²=0.67
10 12 14 16 18 20 22
B. TSURF (°C)
All depths: adj.r²=0.63
<3 meters: adj.r²=0.39
>3 meters: adj.r²=0.41
0 5 10 15 20
C. TBOT (°C)

Figure 6.

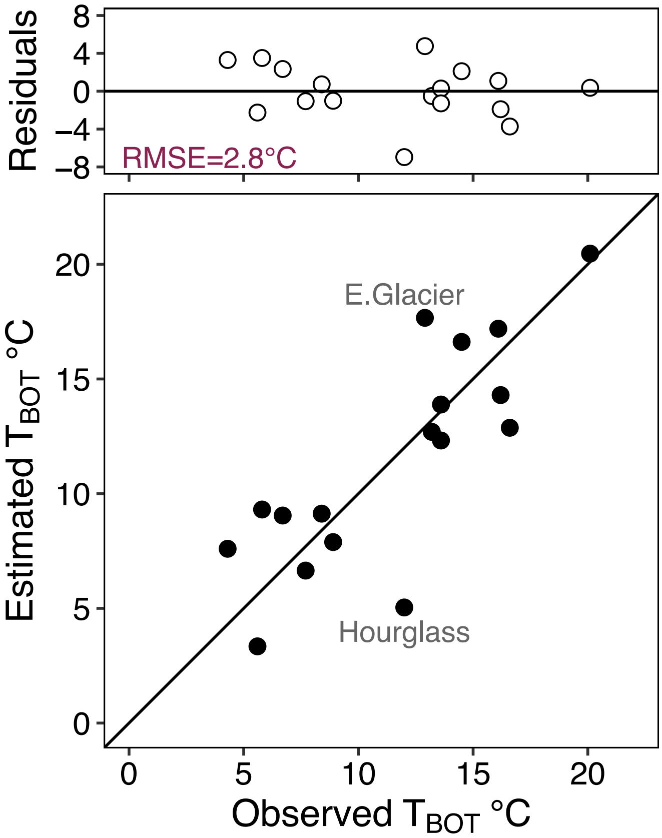

Residuals
8
4
0
−4
−8
RMSE=2.8°C
Estimated T_{BOT} °C
20
15
10
5
0
E.Glacier
Hourglass
0
5
10
15
20
Observed T_{BOT} °C

Figure 7.

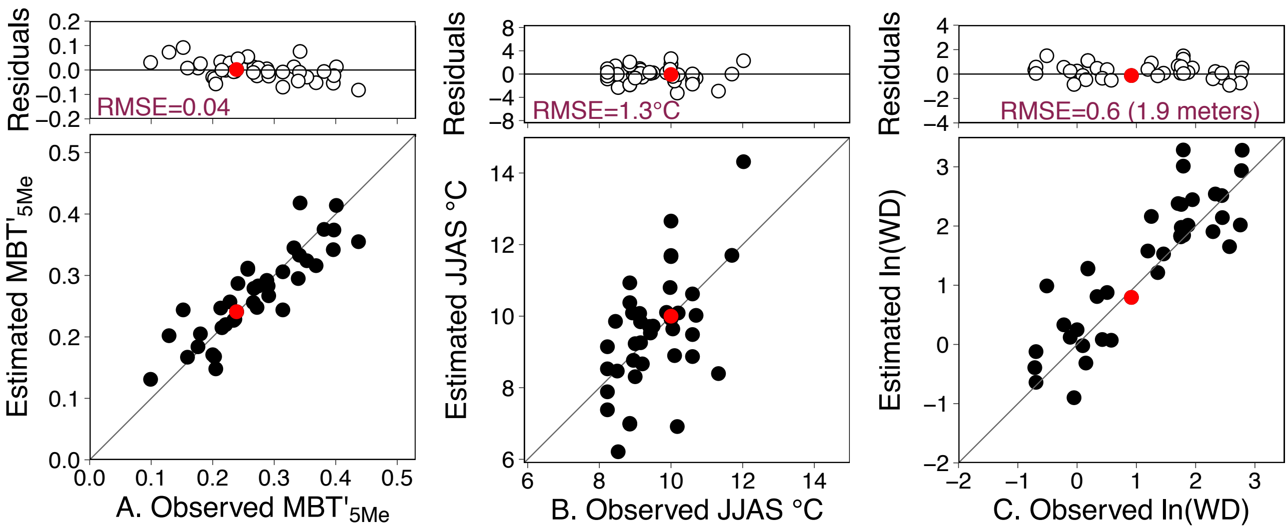
Residuals
RMSE=0.04
Estimated MBT'5Me
A. Observed MBT'5Me
Residuals
RMSE=1.3°C
Estimated JJAS °C
B. Observed JJAS °C
Residuals
RMSE=0.6 (1.9 meters)
Estimated ln(WD)
C. Observed ln(WD)

Figure 8.

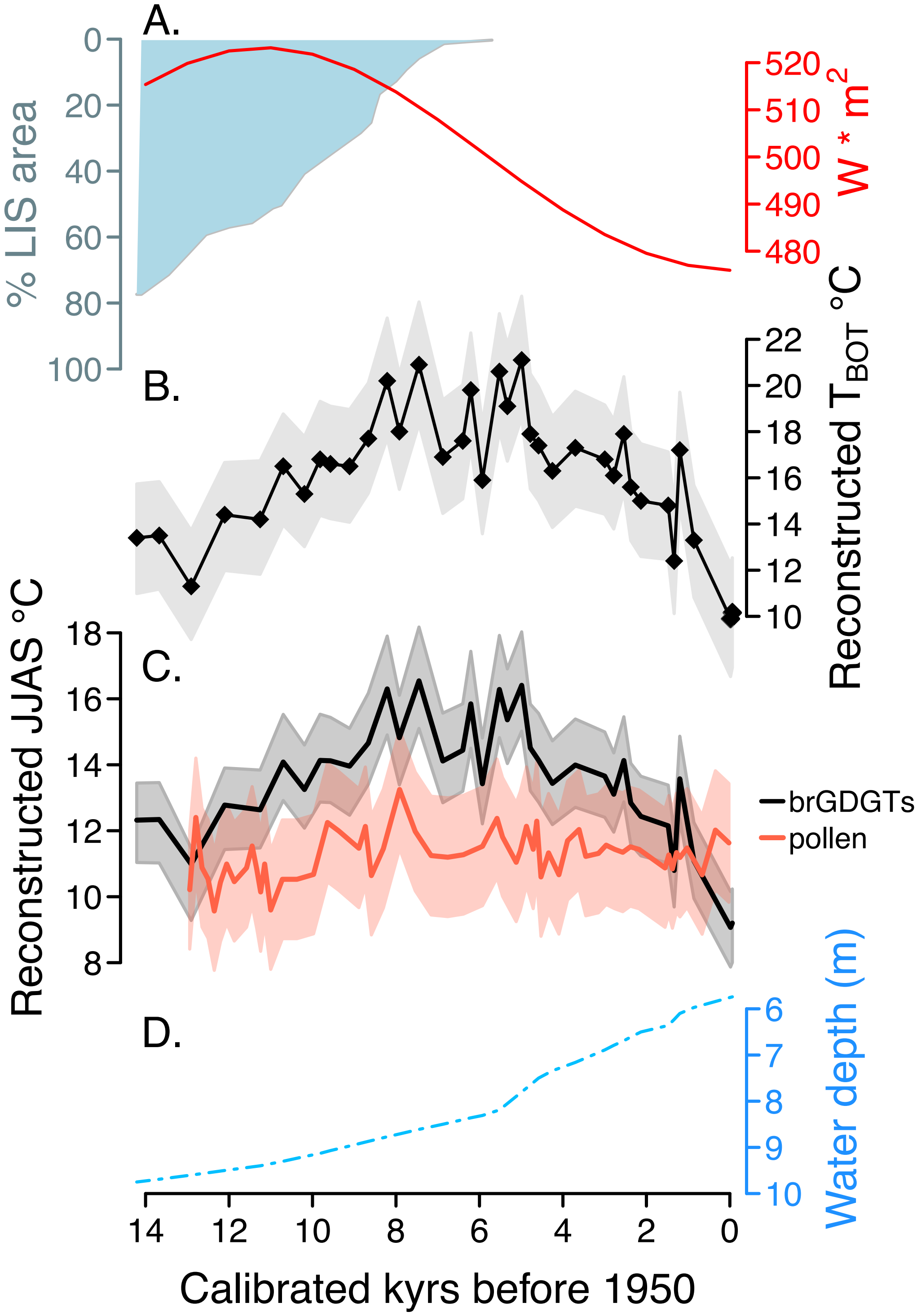
A.
% LIS area
0
20
40
60
80
100
520
510
500
490
480
W * m2
B.
22
20
18
16
14
12
10
Reconstructed TBOT °C
C.
Reconstructed JJAS °C
18
16
14
12
10
8
brGDGTs
pollen
D.
6
7
8
9
10
Water depth (m)
14
12
10
8
6
4
2
0
Calibrated kyrs before 1950

Figure 9.

Supplementary material

Supplementary Table 1. Dissolved oxygen concentrations and pH

Lake	Latitude	Longitude	Elevation (m)	Maximum depth (m)	Sample water depth (m)	Dissolved oxygen mg/L		pH	
						top	bottom	top	bottom
Brooklyn	41.373°N	106.249°W	3233	11.6	11.6	7.37	8.36	8.4	7.0
Crater	41.491°N	106.247°W	3001	19.8	16	7.45	0.01	8.2	7.0
East Glacier	41.377°N	106.259°W	3312	7.6	6	7.21	5.21	7.7	6.9
Fire Box	41.442°N	106.193°W	2935	1	0.5	8.87	8.87	6.8	7.7
Highway 130	41.351°N	106.264°W	3201	1.5	0.8	7.7	7.7	8.7	8.7
Hourglass	41.350°N	106.271°W	3214	1.2	1.1	7.45	7.45	8.9	8.9
Lewis	41.359°N	106.296°W	3311	10.1	9.9	7.54	3.73	7.9	6.3
Libby	41.354°N	106.298°W	3297	12.2	10.3	7.38	0.93	7.8	6.4
Lost	41.445°N	106.118°W	2819	1	0.6	5.6	6.69	7.4	7.0
Mirror Lake	41.338°N	106.320°W	3241	15.7	15.7	7.3	0.47	7.7	6.3
North Banner	41.415°N	106.358°W	3040	4.2	3.3	8.03	12.1	7.9	8.0
Round	41.359°N	106.269°W	3249	1.2	1.2	7.57	7.57		
Silver	41.309°N	106.357°W	3191	7.6	7	7.36	0.17	7.9	6.5
Silver Run	41.327°N	106.237°W	3068	4.3	4.3	8.23	7.61	9.6	9.7
South Gap	41.369°N	106.299°W	3369	21.3	16.2	8.06	3.23	8.7	6.0
Stamp Mill	41.350°N	106.381°W	3039	3.9	3.9	6.15	6.15	6.9	6.4

Supplementary Table 2. Radiocarbon analyses

Core	Depth (m)	Thickness (cm)	Lab No.	Material	^{14}C yr B.P.	Error (yr)	Calibrated age range B.P.		
							5%	Median	95%
LCA	29.5	1	UCIAMS-OS-95575	Bulk	1200	25	1080	1123	1171
LCA	69.5	1	UCIAMS-OS-95576	Bulk	1670	25	1537	1571	1603
LCA	70.5	2	UCIAMS-106149	Charcoal 0.17 mg C	1305	15	1187	1262	1283
LCA	134.5	2	UCIAMS-106150	Charcoal 0.16 mg C	3240	15	3443	3455	3473
LCA	167.5	1	UCIAMS-OS-95573	Bulk	4030	30	4439	4485	4527
LCA	189.5	1	UCIAMS-OS-95574	Bulk	4160	30	4628	4705	4821
LCA	252.5	2	UCIAMS-106151	Charcoal 0.067 mg C	4905	40	5598	5635	5655
LCA	371.5	1	UCIAMS-OS-95572	Bulk	10150	40	11729	11829	11968
LCA	372.5	2	UCIAMS-106152	Charcoal 0.14 mg C	10100	25	11620	11711	11767
LCA	393.5	1	UCIAMS-OS-95577	Bulk	11650	45	13409	13496	13580
LCA	402.5	1	UCIAMS-OS-95598	Bulk	11350	50	13168	13229	13286
LCA	461.5	1	UCIAMS-OS-95603	Bulk	17050	130	20069	20244	20423

Supplementary Table 3. Downcore ages, MBT'_{5Me} values, mean summer air temperature (JJAS) and summer lake bottom temperature reconstructions at Lower Paintrock Lake, WY.

	Calibrated age range B.P.				Estimated JJAS°C			Estimated temperature bottom °C		
Depth (cm)	Median	5%	95%	MBT'_{5Me}	Median	25%	75%	Median	25%	75%
0.5	-59	-68	9	0.219	9.2	8.1	10.3	10.2	7.8	12.5
1.5	-16	-50	343	0.215	9.1	8.0	10.1	9.9	7.4	12.3
23.5	862	294	1070	0.274	11.1	10.0	12.2	13.3	7.1	19.5
36.5	1200	1098	1406	0.344	13.6	12.5	14.8	17.2	11.2	23.8
49.5	1334	1143	1513	0.261	10.8	9.7	11.9	12.4	6.3	18.5
62.5	1477	1185	1576	0.300	12.1	11.1	13.4	14.8	8.7	21.0
76.5	2132	1720	2824	0.306	12.4	11.3	13.7	15.0	9.1	21.5
87.5	2375	1871	3103	0.316	12.8	11.7	14.1	15.6	9.7	22.1
95.5	2540	1980	3201	0.354	14.1	13.0	15.5	17.9	11.8	24.4
105.5	2782	2133	3293	0.323	13.1	12.0	14.3	16.1	10.0	22.4
115.5	2997	2331	3361	0.337	13.7	12.5	15.0	16.8	10.8	23.3
142.5	3703	3505	4202	0.345	14.0	12.9	15.4	17.3	11.1	23.9
160.5	4252	3769	4436	0.327	13.4	12.3	14.7	16.3	10.1	22.7
176.5	4584	4488	4719	0.347	14.1	12.9	15.6	17.4	11.4	24.0
191.5	4782	4647	5029	0.356	14.5	13.4	15.9	17.9	12.1	24.5
206.5	4988	4743	5406	0.410	16.4	15.0	18.1	21.1	14.9	28.1
231.5	5331	4929	5585	0.378	15.4	14.1	16.9	19.1	13.0	25.7
245.5	5522	5130	5650	0.403	16.3	15.0	17.9	20.6	14.1	27.6
257.5	5930	5672	7381	0.320	13.4	12.3	14.7	15.9	9.9	22.3
262.5	6207	5732	7964	0.389	15.8	14.5	17.4	19.8	13.7	26.3
266.5	6400	5780	8288	0.348	14.4	13.3	15.8	17.6	11.5	24.3
276.5	6879	5901	9122	0.338	14.1	12.9	15.6	16.9	10.9	23.5
287.5	7449	6044	9627	0.407	16.5	15.2	18.1	20.9	14.5	27.9
297.5	7919	6199	10132	0.356	14.8	13.6	16.3	18.0	11.9	24.5
303.5	8210	6353	10332	0.398	16.3	14.9	17.8	20.2	14.1	27.0
313.5	8663	6570	10648	0.350	14.7	13.4	16.1	17.7	11.5	24.1
323.5	9112	6964	10879	0.331	14.0	12.8	15.3	16.5	10.4	22.9
333.5	9571	7319	11113	0.334	14.1	12.9	15.5	16.6	10.8	23.2
339.5	9818	7669	11226	0.335	14.1	12.9	15.5	16.8	10.9	23.4
346.5	10194	8037	11342	0.308	13.3	12.1	14.6	15.3	9.2	21.6
356.5	10701	8512	11505	0.330	14.1	12.9	15.4	16.5	10.2	22.9
366.5	11256	9713	11658	0.289	12.6	11.5	13.9	14.2	8.2	20.4
376.5	12105	11817	12913	0.292	12.8	11.7	14.0	14.4	8.2	20.5
386.5	12907	12133	13313	0.239	11.0	9.9	12.1	11.3	5.1	17.5
395.5	13673	13484	14306	0.278	12.3	11.3	13.5	13.5	7.4	19.8
401.5	14212	13611	15584	0.278	12.3	11.3	13.5	13.4	7.0	19.6

Supplementary Table 4. Pollen inferred mean summer air temperatures (JJAS) and mean annual air temperatures (MAAT) from Lower Paintrock Lake, WY and brGDGT inferred MAAT with the 25^{th} and 75^{th} credible intervals from Lower Paintrock Lake, WY.

Pollen-inferred			BrGDGT-inferred			
Age B.P.	JJAS °C	MAAT °C	Age B.P.	MAAT °C median	MAAT °C 25% C.I.	MAAT °C 75% C.I.
23	11.6	1.7	-59	0.1	-0.9	1.0
346	12.0	2.2	-16	-0.1	-1.0.0	0.9
665	10.7	0.7	862	1.8	0.8	2.8
1026	11.5	1.4	1200	3.9	2.9	5.1
1196	11.2	1.4	1334	1.5	0.5	2.4
1279	11.3	1.4	1477	2.7	1.7	3.7
1377	10.8	0.9	2132	2.9	1.9	4.0
1464	11.3	1.4	2375	3.2	2.2	4.4
1553	10.9	1.1	2540	4.3	3.3	5.6
2175	11.4	1.5	2782	3.4	2.5	4.5
2385	11.5	1.7	2997	3.9	2.9	5.1
2567	11.3	1.5	3703	4.2	3.1	5.4
2758	11.4	1.5	4252	3.7	2.7	4.9
2964	11.6	1.6	4584	4.4	3.3	5.7
3149	11.3	1.4	4782	4.7	3.6	5.9
3453	11.2	1.3	4988	6.3	5.1	7.9
3614	12.0	1.9	5331	5.4	4.2	6.8
3889	11.7	1.7	5522	6.2	5.0	7.7
4097	10.7	0.8	5930	3.7	2.7	4.9
4344	11.3	1.4	6207	5.8	4.7	7.3
4526	10.6	0.7	6400	4.6	3.5	5.9
4626	12.3	2.4	6879	4.4	3.3	5.6
4712	11.4	1.6	7449	6.4	5.2	8.0
4874	12.1	2.3	7919	4.9	3.8	6.2
5022	11.4	1.6	8210	6.2	5	7.7
5120	11.0	1.2	8663	4.7	3.7	6.0
5447	11.8	1.8	9112	4.1	3.1	5.5
5579	12.4	2.5	9571	4.3	3.3	5.6
5927	11.5	1.5	9818	4.3	3.3	5.6
6385	11.3	1.4	10194	3.5	2.6	4.7
6760	11.2	1.3	10701	4.2	3.1	5.5
7159	11.2	1.3	11256	3.0	2.1	4.1
7539	12.0	1.9	12105	3.1	2.2	4.2
7913	13.3	3.3	12907	1.6	0.6	2.6
8302	11.5	1.5	13673	2.7	1.8	3.8
8590	10.6	0.8	14212	2.8	1.8	3.8
8733	12.1	2.2				
8890	11.5	1.5				

Age B.P.	MAAT °C	JJAS °C
9372	12.0	2.2
9641	12.3	2.3
9975	10.7	1.0
10373	10.5	0.7
10723	10.5	0.7
11002	9.6	0.0
11147	11.0	1.4
11243	10.1	0.5
11337	10.8	0.9
11447	11.5	1.6
11581	10.9	1.1
11874	10.5	1.0
12057	11.0	1.6
12207	10.4	1.1
12354	9.6	0.3
12503	10.5	1.1
12649	10.9	1.6
12795	12.4	2.7
12942	10.2	0.8

Note: The RMSE for the pollen MAAT calibration is 1.8°C.

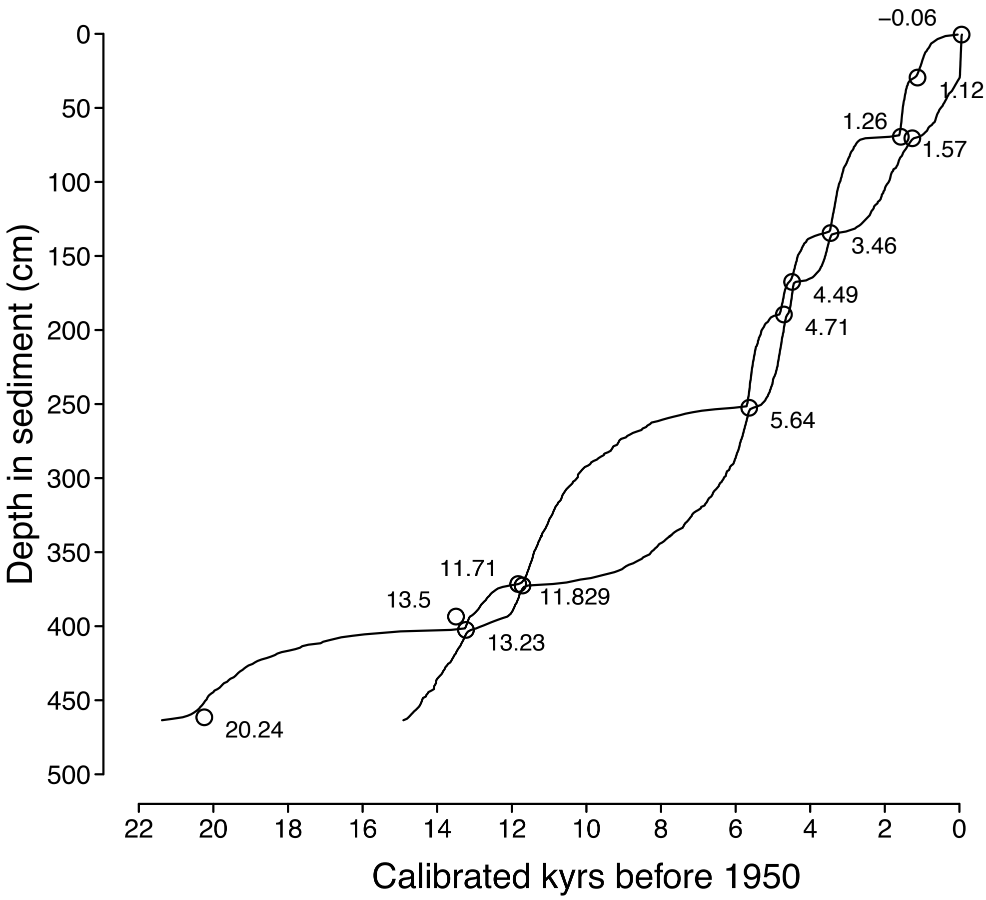

Supplementary Figure 1. Age model versus depth in sediment at Lower Paintrock Lake, WY; radiocarbon ages are shown with open circles while the black lines represent the 90th percent credible intervals of modeled ages.

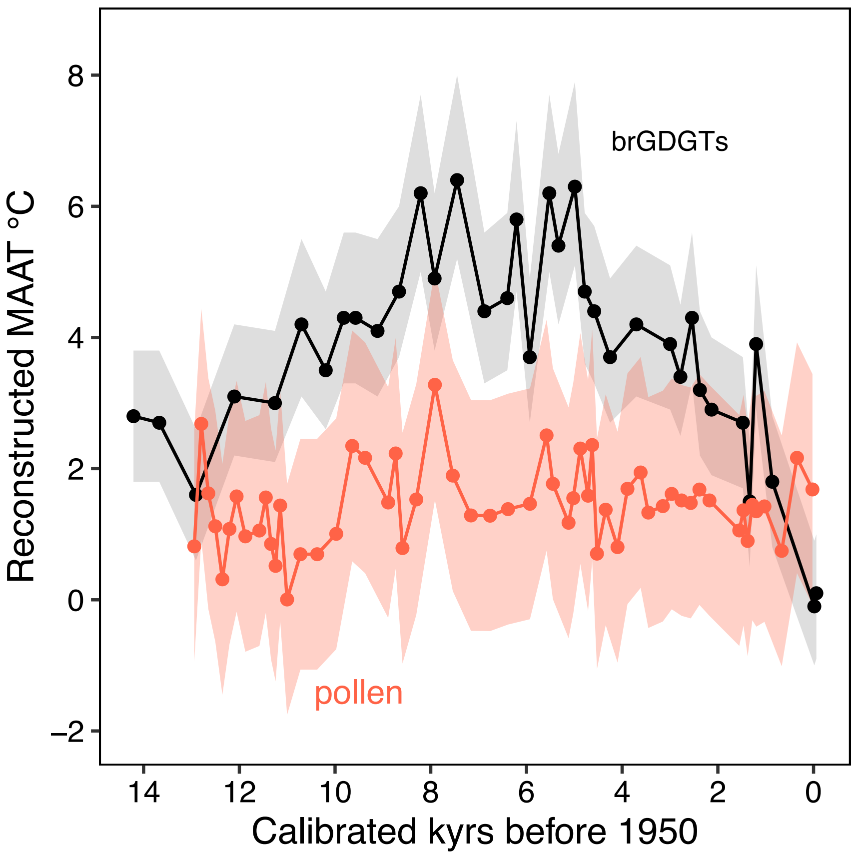

Supplementary Figure 2. Reconstructions of MAAT based on the MBT'$_{5Me}$ index (black line; grey area represents the central 50% C.I.) and pollen (orange line; light orange area represents ±RMSE) from LPR using the same methods employed in the main text. The brGDGT-based reconstructions was generated with the Bayesian calibration listed below.

<u>**Bayesian calibration for MAAT**</u>

The Bayesian calibration model for MBT'$_{5Me}$ as a function of both mean annual air temperature (MAAT) and ln(water depth) at mid-latitude, high-elevation North America is:

MBT'$_{5Me}$ = 0.031 (± 0.009) * MAAT °C - 0.058 (± 0.006) * ln(water depth in meters) + 0.32 (± 0.01)

and error σ^2=0.002 (±0.0005)

where the coefficients and their uncertainties represent the mean and one standard deviation of 4500 iterations of possible slope, intercept and error values generated by the Bayesian regression model.